Local and transboundary contributions to NO_y loadings across East Asia using CMAQ-ISAM and GEMS-informed emission inventory during the winter-spring transition

Jincheol Park, Yunsoo Choi, Sagun Gopal Kayastha

5   Department of Earth and Atmospheric Sciences, University of Houston, Houston, TX, USA

Correspondence to: Yunsoo Choi (ychoi6@uh.edu)

Abstract. We investigated source contributions of nitrogen oxides (NO_x) emissions to reactive nitrogen species (NO_y) loadings across East Asia during the 2022 winter-spring transition. Using the Community Multiscale Air Quality model and
10   its Integrated Source Apportionment Method, we conducted air quality simulations, leveraging top-down estimates of NO_x emissions adjusted by the Geostationary Environment Monitoring Spectrometer tropospheric nitrogen dioxide (NO_2) columns. After the Bayesian inversion, the inventoried NO_x emissions increased by 50% in Korea and 33% in China compared to the a priori estimates, which substantially reduced the model's prior underestimation of surface NO_2 concentrations from -32.75% to -13.01% in Korea and from -10.26% to -3.04% in China. We compared local and
15   transboundary contributions of NO_x emissions to NO_y concentrations across East Asia. Local contributions showed a declining trend, from 32%-43% in January to 23%-30% by May, while transboundary contributions consistently increased from 16%-33% in January to 27%-37% by May. North China consistently contributed over 10% to East Asia's NO_y loadings. East China and South Central China were significant contributors to each other's NO_y budget by 9%-12%. South Central China transboundary contributions consistently outweighed local contributions by 5%, indicating vulnerability to pollution
20   transport. Korea, initially the least influential, contributed 1%-4% to transboundary NO_y concentrations in January. This increased to 6%–7% by May, becoming comparable to other regions' contributions. These behaviors of NO_y were driven by distinct synoptic settings, where strong wintertime northwesterly winds directed pollutants southeastward, while their weakening in spring led to more multidirectional transport patterns, allowing pollutants to spread more broadly across the regions.

25   **1 Introduction**

Nitrogen oxides (NO_x) emissions have long been a significant concern in East Asia due to their detrimental impact on air quality and public health, particularly in densely populated urban areas (Hoek et al., 2013; Newell et al., 2018). NO_x is also a major precursor of secondary aerosols, contributing to the formation of fine particulate matter ($PM_{2.5}$), exacerbating airborne health risks. NO_x has a relatively short atmospheric lifetime, typically ranging from a few hours (Beirle et al., 2011; Lin et al.,

30   2012; Liu et al., 2016; Lange et al., 2022) to several days (Tang et al., 2023; Goldberg et al., 2024), depending on meteorological conditions and chemical regimes in the region. Despite this, NO_x plays a significant role in transboundary pollution. For instance, NO_x emissions from China have been shown to substantially contribute to air quality in Korea during transboundary transport episodes, driven by specific meteorological conditions and chemical regimes in the region. During its transport across the Yellow Sea, NO_x undergoes chemical reactions, forming secondary aerosols and contributing to

35   elevated particulate matter concentrations in Korea (Nault et al., 2018; Eck et al., 2020; Jordan et al., 2020). Furthermore, NO_x rapidly transforms into longer-lived reactive nitrogen species, collectively known as NO_y, which can be transported across long distances. NO_y species, such as nitric acid (HNO_3), nitrous acid (HONO), and peroxyacetyl nitrate (PAN), play a significant role in redistributing nitrogen across extensive regions (Hertel et al., 2012). This extends the impact of NO_x emissions beyond their sources, contributing to both local and transboundary air quality challenges.

40   The transport of air pollutants across Asia, particularly pronounced during the winter-spring transition, is largely determined by shifting synoptic systems that influence both the direction and extent of pollutant movement. In winter, the Siberian High dominates the region, maintaining cold, stable high-pressure systems that drive strong northerly and northwesterly winds (Hui, 2007; Kim et al., 2013; Wyrwoll et al., 2016; Dong et al., 2020). These winds typically result in southeastward and southward pollutant transports, carrying air pollutants from densely industrialized areas in northern China toward downwind

45   regions such as other parts of China, Korea, Southeast Asia, and Japan (Ikeda et al., 2015; Chen et al., 2021; Wu, 2021; Zhao et al., 2021; Kang et al., 2024). As winter progresses into spring, the Siberian High weakens, and while this leads to weaker northwesterly winds, the directionality of pollutant transport becomes more complex due to changes in synoptic patterns. Spring introduces slowly traveling high and low-pressure systems along with shifting wind directions, leading to multi-directional movements of air pollutants across Asia (Peterson et al., 2019). This seasonal transition, along with enhanced

50   vertical mixing from warmer air temperatures and weaker subsidence, allows pollutants to disperse more readily within the boundary layer, facilitating their transport across extended distances (Ryu and Min, 2024). This complexity makes it difficult to fully understand how region-specific pollutant emissions contribute to air quality across Asia, complicating efforts to develop effective air quality management strategies.

To better understand the transboundary behaviors of air pollutants, chemical transport models (CTMs) have been widely

55   used. CTMs, such as the Community Multiscale Air Quality (CMAQ) model (Byun and Schere, 2006), translate emissions inputs and underlying meteorology into three-dimensional representations of air pollutant loadings. This enables simulations of local and transboundary air pollution dynamics, providing insights into the origins and transport pathways of air pollutants. For example, Dong et al. (2020) conducted source apportionment of surface $PM_{2.5}$ concentrations in the Beijing-Tianjin-Hebei (BTH) region, northern China, using CMAQ and its Integrated Source Apportionment Method (CMAQ-ISAM). From

60   2014 to 2017, annual mean $PM_{2.5}$ concentrations decreased by 33%, with local emissions reductions accounting for 47%, intra-regional transport contributing 25%, and transport from outside the region contributing 28%. The contribution of

regional transport increased by up to 40% during spring and winter, driven by strong northwesterly winds. Bae et al. (2020) investigated the influence of NO_x and sulfur dioxide (SO_2) emissions from China on $PM_{2.5}$ concentrations in the Seoul Metropolitan Area (SMA) of Korea during the years 2012 to 2016, using CMAQ. Long-range transport of NO_x and SO_2, which served as precursors for secondary aerosols such as nitrate and sulfate, significantly contributed to aerosol loadings in the SMA. Nitrate aerosols, in particular, comprised 50% of $PM_{2.5}$ during winter and 67% during spring, underscoring their significant share of $PM_{2.5}$ pollution in the SMA during these seasons. Similarly, Lee et al.'s study (2020) demonstrated that the long-range transport of $PM_{2.5}$ and its precursors, including NO_x, SO_2, and volatile organic compounds (VOCs), originating from China led to substantial increases in $PM_{2.5}$ concentrations in Korea by up to 50% during the 2016 KORUS-AQ campaign period. Tang et al. (2023) also assessed the contributions of local and transboundary emissions to $PM_{2.5}$ concentrations in Korea during the 2016 KORUS-AQ campaign. Under stagnant high-pressure conditions, local emissions were the dominant source, accounted for up to 49% of $PM_{2.5}$ concentrations in the SMA. However, during periods of strong westerly winds, pollutants transported from China significantly impacted air quality in the SMA, contributing as much as 71% of $PM_{2.5}$ concentrations. Kashfi Yeganeh et al. (2024) quantified the contributions of transboundary NO_x and VOC sources to ozone concentrations in Seoul, Korea, during a June 2019 ozone exceedance event. Ozone precursors were transported by northwesterly and westerly winds from China, accounting for 57.7% of the ozone concentrations in Seoul, while local emissions contributed 42.3%. Beyond the studies mentioned above, a number of CTM-driven source apportionment efforts have highlighted the substantial contributions of both local and transboundary pollutants to air quality across Asia (Kajino et al., 2013; Wang et al., 2015; Li et al., 2017a; Li et al., 2019; Shen et al., 2022; Xian et al., 2024). While such earlier efforts have provided valuable insights into Asia's pollution dynamics influenced by prevailing winds and dominant emission sources, the extent of source contributions varied across the regions due to differences in the materials and methods employed in each study. A common issue highlighted in many of these studies is the uncertainty in emission inventories, which can compromise the reliability of simulations. This often stems from the use of incomplete or outdated emission inventories, as pointed out in several previous studies (Carmichael et al., 2002; Pan et al., 2014; Sargent et al., 2021; Russo, 2019; Han et al., 2021; Liu et al., 2021a), which may not effectively reflect current emission sources, industrial developments, or recent advancements in pollution control.

In response to the need for more accurate air quality simulations, which are essential for proceeding with further analyses based on their outcomes, extensive efforts have been made to refine emission inventories across Asia. Traditional bottom-up methods, such as ground surveys and industrial reporting, however, can be time-consuming and often outpaced by rapidly evolving emissions patterns, making them less reflective of contemporary emissions activities (Placet et al., 2000; Rypdal and Winiwarter, 2001; Li et al., 2021; Smith et al., 2022). To address this, satellite observation data have widely been used to update emission inventories in a top-down manner, taking advantage of the instruments' broader geographic coverage. Instruments aboard sun-synchronous low Earth orbit satellites, such as the Ozone Monitoring Instrument (OMI) and the TROPOspheric Monitoring Instrument (TROPOMI), have been particularly effective in constraining the extent of air

95   pollutant emissions. More recently, the Geostationary Environment Monitoring Spectrometer (GEMS) has further enhanced this process by capturing daytime variations in pollutant loadings, such as tropospheric nitrogen dioxide (NO_2) columns, offering unprecedented insights into the diurnal behaviors of pollutants across Asia. Leveraging the top-down information, a number of studies have successfully refined Asia's emission inventories, achieving substantial improvements in CTM-based simulation accuracy (Itahashi et al., 2012; Yumimoto et al., 2014; Goldberg et al., 2019; Souri et al., 2020; Li et al., 2021b;

100 Jung et al., 2022; Son et al., 2022; Feng et al., 2023; Mun et al., 2023; Park et al., 2023; Momeni et al., 2024; Park et al., 2024). However, only a few have extended their scope to utilize these refined simulations for further analyses of cross-regional pollutant dynamics across multiple seasons; updating emission inventories itself is already a resource-intensive process, demanding a series of forward model runs and iterative adjustments. For example, Souri et al. (2020) refined NO_x and VOC emissions across East Asia during the 2016 KORUS-AQ campaign period, through analytical inversion using

105 satellite data from OMI and Ozone Mapping and Profiler Suite Nadir Mapper (OMPS-NM) and CMAQ. The inversion led to significant reductions in NO_x emissions by 22%-41% in China, Taiwan, and Malaysia, while Korea and Japan showed increases by 9%-12%. VOC emissions over the North China Plain were adjusted upward by 25%, a significant increase compared to the previously reported 5% since 2010. This involved shifts in chemical regimes across East Asia, with regions transitioning between NO_x-sensitive and VOC-sensitive conditions, providing more recent insights into ozone formation

110 risks across different regions. Similarly, Jung et al. (2022) refined East Asia's NO_x emission inventory for spring 2019 through Bayesian inversion using TROPOMI data and CMAQ-ISAM. The use of more up-to-date emissions substantially reduced model biases in simulating NO_2, ozone, and $PM_{2.5}$ concentrations, revealing that the prior emissions were underestimating the contributions of transboundary pollutants. NO_x emissions from neighboring regions contributed 22.96%–35.24% to local NO_x budgets and 24.23%–42.26% to ozone budgets in both China and Korea, reaffirming the

115 critical role of anticyclonic systems over the Yellow Sea in driving pollutant transport. Despite these efforts, there is still a need for more rigorous efforts in this domain to better explore regional pollution dynamics. Particularly, the recurrent pollutant patterns during East Asia's winter and spring seasons deserve updated perspectives on the complex interplay between evolving synoptic systems and pollutant transport dynamics, which significantly affect air quality across the region.

Leveraging top-down estimates of NO_x emissions informed by GEMS tropospheric NO_2 columns, followed by improved

120 accuracy in CTM simulations, our study aims to conduct a comprehensive source apportionment of East Asia's NO_y concentrations during the winter-spring transition in 2022. First, we applied diurnal updates to the inventoried extent of NO_x emissions using GEMS NO_2 columns as top-down constraints during the Bayesian inversion, enabling CMAQ to more accurately simulate NO_y concentrations. Then, using CMAQ-ISAM, we quantified the local and transboundary contributions of NO_x emissions to NO_y concentrations across five major NO_x source regions of East Asia during the period from January

125 to May 2022. By capturing the response of pollutants to evolving seasonal dynamics, we assessed the source-receptor interplays between the regions, aiming to provide more up-to-date insights into the broader cross-regional pollution transport dynamics.

2 Data and Methods

2.1 Model simulations

130 Meteorology governs the dispersion and transport of air pollutants, making it a critical factor in CTM simulations. We used the Weather Research and Forecasting (WRF) model 3.8.1 (Skamarock et al., 2008) to simulate meteorological fields over the modeling domain (Fig. 1). The simulation spanned from January 1 to May 31, 2022, covering East Asia's winter and spring seasons. We simulated hourly meteorological fields over a 320×320 grid with 35 vertical layers at a spatial resolution of 27 km and then converted them into a CMAQ-compatible format using the Meteorology-Chemistry Interface

135 Processor (MCIP). We used the Morrison two-moment scheme for microphysics (Morrison et al., 2009), the Rapid Radiative Transfer Model for GCMs (RRTMG) for longwave and shortwave radiation (Clough et al., 2005; Iacono et al., 2008), and the Pleim-Xiu land surface and surface layer models (Xiu and Pleim, 2001; Pleim, 2006). Planetary boundary layer processes were simulated using the ACM2 model (Pleim, 2007a; Pleim, 2007b), and cumulus parameterization was handled by the Kain-Fritsch scheme (Kain, 2004). We applied the Four-Dimensional Data Assimilation (FDDA) grid-nudging option (Jeon

140 et al., 2015) for meteorological inputs. Initial and boundary conditions were derived from the National Centers for Environmental Prediction (NCEP) FNL operational model global tropospheric analysis.

Using the WRF-simulated meteorology and established emissions as inputs, CMAQ simulates the behavior and distribution of pollutants in the atmosphere in a three-dimensional manner. We employed two different versions of CMAQ: CMAQ 5.2 with its Decoupled Direct Method in Three Dimensions (CMAQ DDM-3D) as a forward model in the emission adjustment

145 process, and CMAQ 5.3.2 with its ISAM for performing source apportionment. CMAQ DDM-3D calculates the first-order coefficients that represent locally semi-normalized sensitivities of modeled pollutant concentrations to changes in relevant emissions input (Napelenok et al., 2006). CMAQ-ISAM tags pollutants emitted from user-defined source regions, and then tracks them through atmospheric processes such as advection, chemical transformation, and deposition (Kwok et al., 2015). This allows for quantifying the contribution of specific emission sources to pollutant loadings at receptor locations across the

150 modeling domain, offering detailed insights into source attribution. Building upon previous studies conducted in Asia (Jung et al., 2022; Park et al., 2023; Park et al., 2024), we employed CMAQ configurations that have been validated in comparable contexts across the region. Using CMAQ DDM-3D, we simulated hourly NO_2 concentrations over a 300×300 grid and obtained their corresponding sensitivities to NO_x emissions, which were used for the Bayesian inversion to constrain the inventoried extent of NO_x emissions (details in Sect. 2.2 and 2.4). We used the YAMO scheme and the WRF omega formula

155 for solving horizontal advection and vertical advection, respectively. Horizontal diffusion was modeled using the multiscale approach, and vertical diffusion was represented with the ACM2 vertical diffusion scheme (Pleim, 2007a; Pleim, 2007b). Gas-phase chemistry was solved using the Carbon Bond 05 (CB05) mechanisms for CMAQ DDM-3D and CB6 for CMAQ-ISAM. Aerosol processes were modeled using the AERO6 module, and dry deposition was estimated using the M3Dry scheme (Pleim, 2007b). We used static boundary conditions during the entire simulation period. Using CMAQ-ISAM, we

160 quantified the local and transboundary contributions of NO_x emissions to NO_y concentrations among five selected regions (Fig. 1), including Korea, Northeast China, North China, East China, and South Central China. In our discussion of Korea (later in Sect. 3), we focused on the SMA, the country's economic hub, where dense traffic activity contributes to severe air pollution, as highlighted in the small panel of Fig. 1, which illustrates its geographic extent. North Korea, despite its close proximity to these regions and the potential impact of its emissions on neighboring regions' air quality, was excluded from

165 our study. This was primarily due to the uncertainty in North Korea's emissions, which warrants a dedicated study of its own. Global emission inventories like EDGAR rely on accurate energy usage data to estimate pollutant emissions, and the lack of reliable input data for North Korea made it impractical to include as a separate source region in this study. Our focus was on total NO_y concentrations within the PBL at receptor regions rather than surface NO_x or NO_2 concentrations due to the latter's short atmospheric lifetimes, which limit their long-range transport. The PBL facilitates the most efficient mixing and

170 transport across regions, making it an ideal layer for assessing cross-regional behaviors of pollutants (Li et al., 2017b). However, it is important to acknowledge that substantial pollutant transport also occurs in the free troposphere beyond the PBL, where stronger winds facilitate long-range transport of pollutants. Our study specifically focuses on the PBL to assess cross-regional pollutant behaviors, as this layer directly influences surface air quality, the modeled estimates of which can be evaluated with station measurements (detailed in Sect. 2.5), and human health associated. We quantified the extent to which

175 NO_y remained near local sources versus how much was transported to neighboring receptor regions during the winter-spring months. Note that we used the summation of NO_x, nitric acid (HNO_3), nitrous acid (HONO), and peroxyacetyl nitrate (PAN) to represent NO_y, capturing the major reactive nitrogen species that contribute to total NO_y concentrations during the simulations. Both the WRF and CMAQ simulations began with a 10-day spin-up from December 22 to December 31, 2021. Further technical details of our modeling setup are listed in Table S1.
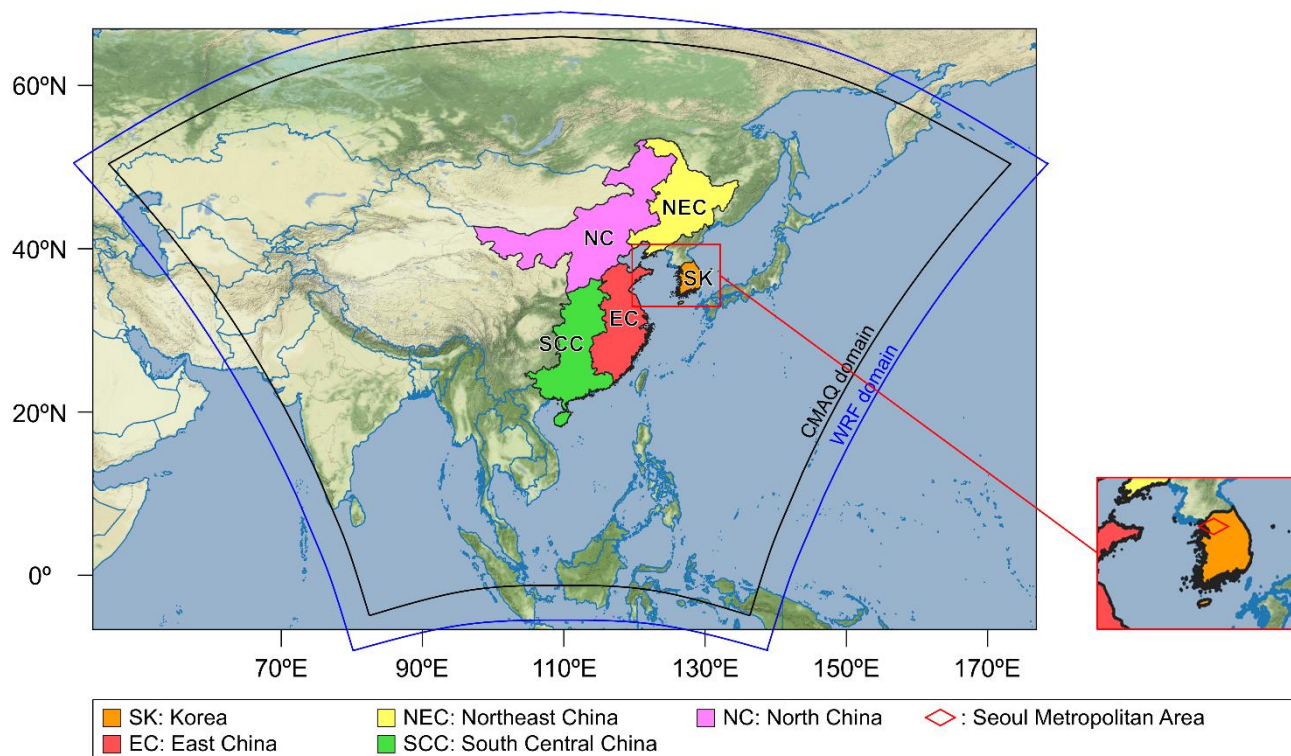
Figure 1: Modeling domain and five source apportionment regions across East Asia.

2.2 Emission inventories

Emission inventories provide CTMs with spatiotemporally resolved information on the extent of air pollutant emissions, enabling the simulation of their behavior and resulting concentrations in the atmosphere. We prepared anthropogenic emissions over the modeling domain using the Emissions Database for Global Atmospheric Research (EDGAR) 6.1 (Crippa et al., 2020), which offers annual data (base year: 2018) for greenhouse gas and air pollutant emissions at a 0.1° spatial resolution. We processed these emissions into a CMAQ-compatible format using the Sparse Matrix Operator Kernel Emissions (SMOKE) 4.7 modeling system (Houyoux et al., 2000). This process involved re-gridding the emissions into a 27 km resolution and allocating the annual lumped emissions into hourly speciated emissions for the period from January 1 to May 31, 2022, while accounting for time zones and weekday weekend profiles that vary across geographical locations. It is noteworthy that, unlike our previous study (Park et al., 2023) and other literatures that inspired our methodology (Souri et al., 2020; Jung et al., 2022), we did not use the 2016 KORUS-AQ emission inventory (version 5) developed by Woo et al. (2020). This inventory, widely adopted for Asia-focused studies, was delicately built upon a combination of multiple regional surveys, providing comprehensive representations of emissions patterns across Asia. However, since the KORUS-AQ inventory provides the inventoried extent of pollutant emissions as monthly and yearly totals and given the requirements

of our inversion method (detailed in Sect. 2.4) to update Asia's emission inventory on an hourly basis, we used the EDGAR inventory instead. The EDGAR database offers region-specific hourly emissions profiles, allowing us to avoid introducing additional uncertainties associated with the temporal allocation of monthly emissions into hourly emissions. We prepared biogenic and biomass burning emissions using the Model of Emissions of Gases and Aerosols from Nature (MEGAN) 3.0 (Guenther et al., 2018) and the Fire Inventory from the National Center for Atmospheric Research (NCAR) (FINN) 1.5 (Wiedinmyer et al., 2011). MEGAN estimates the extent of gases and aerosol emissions from terrestrial ecosystems based on vegetation responses to meteorological conditions. We obtained hourly biogenic emissions at a 27 km resolution using the WRF-simulated meteorological fields and Leaf Area Index (LAI) averaged over vegetative surfaces (referred to as LAIv) as an input, which can be calculated by dividing grid-specific LAI by the fraction of each grid cell covered by vegetation (Guenther, 2006). To calculate LAIv, we used the Reprocessed Moderate Resolution Imaging Spectroradiometer (MODIS) Version 6 LAI product (Yuan et al., 2011) and the Visible Infrared Imaging Radiometer Suite (VIIRS) global Green Vegetation Fraction product (Jiang et al., 2016), following the method established in previous studies (Jung et al., 2021; Park et al., 2022). This ensures that MEGAN estimates biogenic emissions based on more contemporary information on vegetative surfaces over the modeling domain. FINN provides emissions from open biomass burning events, such as wildfires, agricultural fires, and prescribed burning, based on satellite observation data and fuel load parameters. We obtained hourly biomass burning emissions at a 27 km resolution, using the Fortran-based gridding program (fire_emis) provided by NCAR, which spatiotemporally allocated FINN emissions into our modeling grid. We merged these anthropogenic, biogenic, and biomass-burning emissions to prepare a comprehensive emissions input for CMAQ (hereafter referred to as the a priori emissions). Note that our use of two different CMAQ versions required species mapping, as EDGAR emissions were provided in the CB05 mechanism, which CMAQ DDM-3D can digest, but CMAQ-ISAM requires those in CB06. We converted the chemical species from CB05 to CB06 using the species mapping method described in a previous study (Collet et al., 2018).

2.3 Satellite data

GEMS is the first ultraviolet-visible geostationary instrument capable of capturing diurnal profiles of both gaseous pollutants and aerosols across the Asia-Pacific region, covering longitudes from 75° E to 145° E and latitudes from 5° S to 45° N (Choi et al., 2018). We used GEMS Level 2 NO_2 product (version 2.0) to obtain a top-down overview of NO_2 loadings across the modeling domain. This product, including observations from November 2020 to the present, provides 6 to 10 consecutive snapshots of NO_2 column densities at hourly intervals during the daytime, at a spatial resolution of 3.5 km × 8 km. For clarification, GEMS provided 6 observations per day from 00:45 to 05:45 UTC in January, 7 observations from 00:45 to 06:45 UTC in February, 8 observations from 23:45 to 06:45 UTC in March, and 10 observations from 22:45 to 07:45 UTC in April and March.

We used tropospheric NO_2 columns observed from January 1 to May 31, 2022, as top-down references for constraining the a priori emissions. In addition to the NO_2 columns, we incorporated several other variables during the inversion process (see Sect. 2.4), including the averaging kernel, cloud fraction, data quality flags, and root mean square error. We also used model-derived variables from the GEMS Level 2 data, including tropospheric and stratospheric air mass factors (AMFs), a priori tropospheric NO_2 profile, and tropospheric pressure profile from the WRF model coupled with Chemistry (WRF-Chem) 3.9.1 (NIER, 2020). To ensure consistency in the vertical distribution assumptions between GEMS tropospheric NO_2 columns and CMAQ-simulated tropospheric NO_2 columns, we recalculated the AMFs using the vertical NO_2 profiles simulated by CMAQ. These AMFs were then used to adjust the GEMS-retrieved NO_2 columns, aligning them with CMAQ's vertical profiles. This process involves interpreting the satellite retrievals using CMAQ's vertical NO_2 profiles instead of the original GEMS a priori vertical profiles, which were based on WRF-Chem. This adjustment ensures that both the NO_2 columns are interpreted consistently with the model vertical structure, thereby mitigating biases introduced by differences in the initial assumptions about the vertical distribution of NO_2. This approach builds upon methods established in previous inverse modeling studies that directly compared OMI- and TROPOMI-derived NO_2 columns with CMAQ simulations (Souri et al., 2016; Souri et al., 2017; Souri et al., 2020; Jung et al., 2022a; Jung et al., 2022b). To ensure data quality, we used pixels with a quality flag of 0 bits (good sample) and cloud fractions below 0.3; note that since the Level 2 data version 2.0 quit employing the OMI climatology thereby deserves further validation efforts through retrieval studies, we excluded the cloudy scenes which could lead to inaccurate AMF references.

2.4 Top-down approach to constrain NO_x emissions

The extent of NO_x emissions is not directly measurable through GEMS's observations, which instead capture NO_2 column densities. While these are closely related to NO_x emissions, they do not provide direct quantitative measurements of the emissions themselves. Therefore, to establish quantitative constraints on NO_x emissions and obtain the updated estimates accordingly, we employed a Bayesian approach for inverse modeling, which is suited for solving problems that are not grossly nonlinear (Rodgers, 2000).

Given the short atmospheric lifetime of NO_2, our approach assumes a local, linear relationship between NO_2 columns and NO_x emissions. This assumption, widely adopted in earlier inverse modeling studies (Martin et al., 2003; Souri et al., 2016, 2018, 2020; Jung et al., 2022a, 2022b; Park et al., 2023, 2024), is based on the understanding that satellite-observed NO_2 columns are most likely to reflect recent, localized NO_x emissions due to NO_2's short atmospheric lifetime. Furthermore, the linearity simplifies the inversion process by directly relating observed column densities to emissions, avoiding the need for computationally intensive modeling of nonlinear processes. However, it is noteworthy that the observed NO_2 columns at any given time are influenced not only by current NO_x emissions but also by NO_2 remaining from previous hours. Additionally, nighttime chemical reactions involving ozone and hydroxyl radicals (OH) can introduce nonlinearity between NO_x emissions and NO_2 concentrations, which is a complexity beyond the scope of our study. Assuming that uncertainties in observations

and emissions follow a Gaussian distribution, our approach aimed to derive the most probable estimate of a posteriori NO_x emissions by integrating prior knowledge (a priori emissions) and top-down observational constraints. This involves minimizing the cost function derived from Bayes's theorem, as shown in Eq. 1 (Rodgers, 2000).

$$J(x) = \frac{1}{2}(y - Fx)^T S_o^{-1}(y - Fx) + \frac{1}{2}(x - x_a)^T S_e^{-1}(x - x_a) \qquad (1)$$

This process determined the a posteriori emissions $\boldsymbol{x}$ for each grid cell, given multiple inputs: the a priori emissions $\boldsymbol{x_a}$, observation constraints $\boldsymbol{y}$ (hourly GEMS NO_2 columns), and CMAQ-simulated NO_2 columns $\boldsymbol{F}$. Due to the 15-minute offset in the availability of GEMS Level 2 products (from 22:45 to 07:45 UTC), we aligned the observations to the nearest subsequent hour (e.g., GEMS data at 04:45 UTC were used to constrain emissions at 05:00 UTC). We assumed emissions uncertainties $\boldsymbol{S_e}$ at 50%, 200%, and 100% for anthropogenic, biogenic, and biomass burning emissions, respectively, based on previous modeling studies conducted across Asia (Souri et al., 2020; Jung et al., 2022; Park et al., 2023; Park et al., 2024). Observation uncertainty $\boldsymbol{S_o}$ was sourced from the GEMS Level 2 data.

Once the first derivative of the cost function reached its minimum, we applied the Gauss-Newton method to iteratively refine the emissions estimate, as shown in Eq. 2. This process involved adjusting the estimate $\boldsymbol{x}$ (with each iteration noted as $\boldsymbol{i}$; $\boldsymbol{i} = 4$ in January, February, and $\boldsymbol{i} = 3$ in March, April, and May), gradually progressing towards a converged solution. The Jacobian matrix $\boldsymbol{K}$, which represents the sensitivity between NO_x emissions and NO_2 concentrations, was calculated by CMAQ DDM-3D at the beginning of the simulations and remained fixed throughout the inversion process. Meanwhile, the forward model $\boldsymbol{F}$ was updated with each iteration, guiding the inversion toward reducing discrepancies between the observed and modeled NO_2 columns.

$$\hat{x}_{i+1} = x_a + S_e K_i^T (K_i S_e K_i^T + S_o)^{-1}[y - Kx_i + K_i(x_i - x_a)] \qquad (2)$$

The inversion was applied whenever the top-down constraints were available, allowing us to constrain hourly NO_x emissions during GEMS's daylight retrieval hours, while keeping nighttime emissions unchanged. We chose not to adjust nighttime emissions primarily due to the absence of observational reference during these hours and also to isolate the daily emission cycle, allowing the model to "pause" and mitigate carry-over effects from the previous day's emissions (Park et al., 2024). However, a limitation of this approach is that it does not improve the representation of nighttime emissions, leaving these unadjusted due to the absence of observational constraints. Consequently, any model biases associated with nighttime emissions remain unresolved.

2.5 Station measurements for model evaluation

Before using the WRF-simulated meteorological fields as input for CMAQ, we evaluated their accuracy against ground-based measurements at weather stations operated by the Korean Meteorological Administration. We used hourly measurements of 2 m air temperature and 10 m wind U and V components from 95 stations, collected for the period from January 1 to May 31, 2022. The modeled meteorology showed fair agreement with station measurements (Fig. S1), with Pearson's correlation coefficients (R) ranging from 0.89 to 0.98 and Index of Agreement (IOA) values between 0.83 and 0.98.

To evaluate the accuracy of CMAQ simulations, we used hourly surface NO_2 and $PM_{2.5}$ concentrations observed at ground-based monitoring stations in Korea and China during the period from January 1 to May 31, 2022, sourced from Korea's Ministry of Environment (AirKorea) and China's Ministry of Ecology and Environment (MEE). To ensure the quality of AirKorea measurements, from an original count of 515 stations, we excluded those with more than 50% missing data during the validation period (Park et al., 2022; Park et al., 2023), which resulted in a 9.68% data loss and retaining 465 stations. To ensure the quality of MEE measurements, we applied data filtering methods to data from 185 national control points, consisting of 20 sites in Northeast China, 38 sites in North China, 78 sites in East China, and 49 sites in South Central China. These control points are strategically distributed across China and managed by its central government to ensure consistent and reliable air quality measurements (Liu et al., 2021a; Liu et al., 2022). We excluded negative values and duplicate records (> 4 consecutive repeats) caused by equipment failures, following the data-filtering methods in previous studies (Rohde, 2015; Silver, 2018; Zhai, 2019). This resulted in a decrease in the number of data points by 0.41% for NO_2 and 0.38% for $PM_{2.5}$, respectively. Note that we converted MEE's NO_2 measurements from its native unit $\mu g/m^3$ to ppb.

3 Results and discussion

3.1 Model evaluation

Prior to proceed with source apportionment, we first evaluated the accuracy of our CMAQ simulations across East Asia. We compared the observed and modeled tropospheric NO_2 columns from using the a priori and a posteriori NO_x emissions, in order to evaluate the improvement in the model's performances. Figure 2 shows monthly averages of hourly daytime NO_2 columns during the period from January to May 2022. The prior model generally underestimated NO_2 columns across North China, Northeast China, and the northern half of East China, and the SMA of Korea (Figs. 2a and 2b). The extent of underestimation was particularly pronounced in North China, failing to capture highly polluted areas observed throughout the simulation period. To a lesser extent, the model sporadically overestimated the columns across South Central China, the southern half of East China, and the rest of Korea except the SMA.

315 After the inversion, there were substantial adjustments to the extent of daytime NO_x emissions across the regions (Fig. S4), seemingly counterbalancing the earlier model under- and overestimation. During the winter-spring months, on average, there were increases in the emissions by 50.12% in Korea, 30.86% in Northeast China, 78.63% in North China, 20.76% in East China, and 2.6% in South Central China (Table S2). Overall, these adjustments led to a closer alignment between the observed and modeled NO_2 columns (Fig. 2c). For example, in regions such as North China, including Beijing, and parts of

320 Northeast China, such as Shenyang, NO_2 columns substantially increased by a factor of approximately 1.2 to 2.0 during winter months (January and February). Similarly, the SMA of Korea experienced moderate increases by a factor of 1.2 to 1.5, during the same period. In contrast, in South Central China, NO_2 columns showed a mix of increases and decreases depending on the month. In May, for instance, NO_2 columns in South Central China decreased by a factor of about 1.3, compensating for the model's earlier overestimation. In addition, we noticed some posterior overcompensation in the

325 modeled columns, shown by some overestimated values across North and South Central China and Korea in February and March, which could have been caused by our use of the Bayesian approach, often regarded as a simple inverse modeling method which cannot fully resolve the non-locality of air pollutants (Park et al., 2024). Nonetheless, overall, our use of the a posteriori NO_x emissions yielded a more accurate spatial representation of NO_2 concentrations across the regions during the winter-spring transition, demonstrating its effectiveness in refining emission inventories and thereby improving model

330 accuracy.

Tropospheric NO₂ columns observed and modeled in Asia
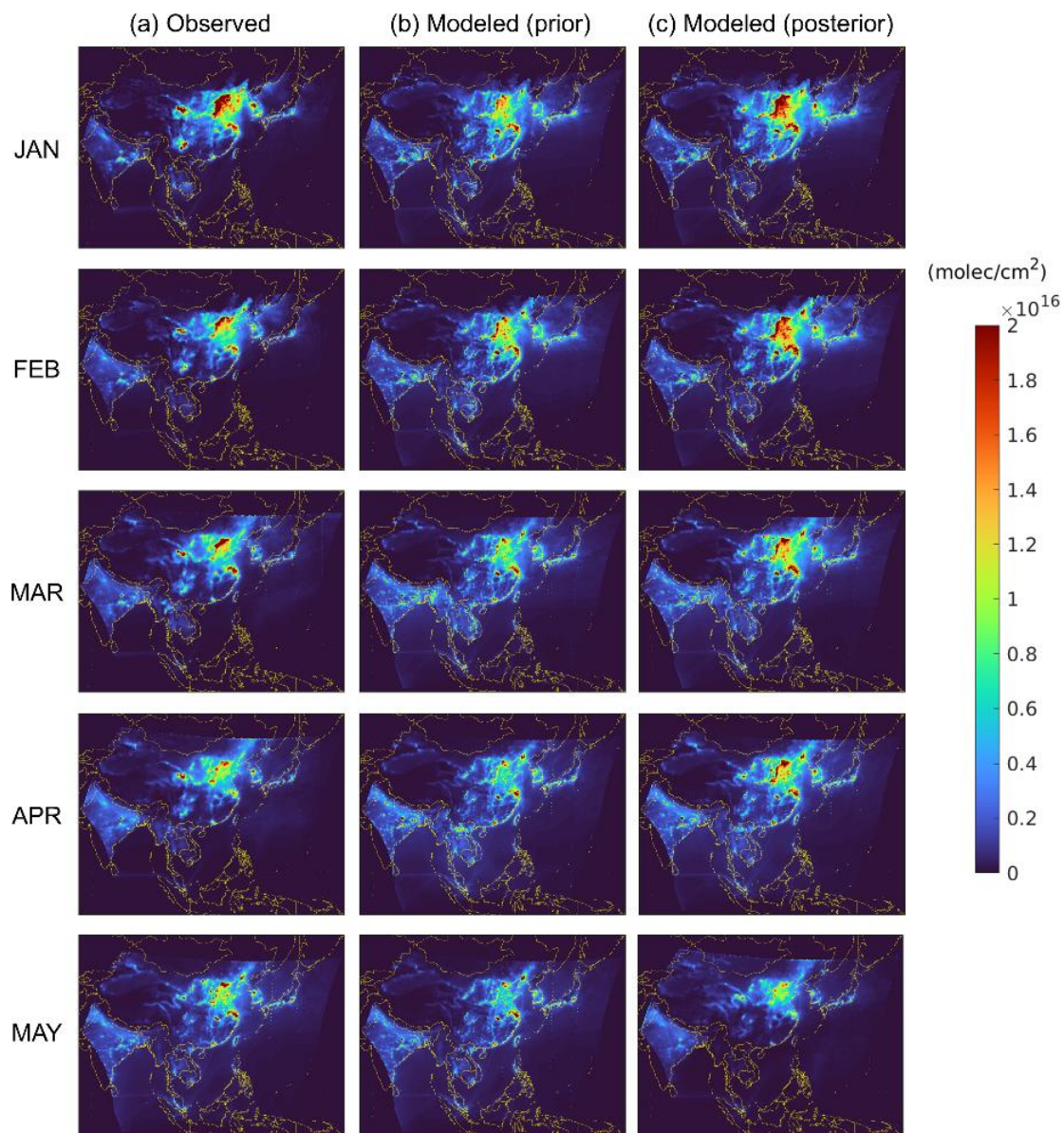
Figure 2: Averages of hourly tropospheric NO₂ columns (molecules/cm²) observed and modeled during daylight hours (GEMS retrieval hours) in each month from January to May 2022. (a) GEMS tropospheric NO₂ columns, (b) modeled NO₂ columns using the a priori emissions, (c) modeled NO₂ columns using the a posteriori emissions. Note that we excluded the modeled columns that do not correspond with the GEMS's retrieval times.

The increases in NO$_x$ emissions reduced the extent of model biases in simulating daytime surface NO$_2$ concentrations from -32.75% to -13.01% in Korea and from -10.26% to -3.04% in China on average (from -39.06% to -9.40% in Northeast China, from -2.78% to 2.76% in North China, from -9.65% to -3.32% in East China, and from -12.41% to -10.92% in South Central China) (Fig. 3; Table 1). This led to closer alignment between the modeled and observed concentrations during the months, showing improvements in R from 0.67 to 0.71 and IOA from 0.71 to 0.82 in Korea, and R from 0.65 to 0.76 and IOA from 0.79 to 0.86 in China. Despite the improvements, the extent of the prior underestimation still remained the largest in January, gradually decreasing as the months progressed to May. This suggests a potential underrepresentation of NO$_x$ emissions in the a priori inventory during the colder months, possibly due to the use of the global emissions database, which may not fully capture localized, high energy usage in those periods. There were instances of overcompensation after the inversion, such as in March and April for North China, as well as in April for East China and May for South Central China, where the prior model's underestimations turned into overestimations (Table 1). This could be attributed to the carry-over effect of NO$_2$ transport from neighboring grid cells, which the Bayesian inversion, which assumes a strictly local relationship between emissions and concentrations, cannot fully constrain (Park et al., 2024). Nevertheless, the reductions in mean absolute errors across these regions suggest an overall improvement in simulation accuracy.

350

Figure 3: Daytime mean surface NO₂ concentrations observed and modeled at ground-based measurement sites within each of the five source apportionment regions across East Asia during the period from January 1 to May 31, 2022. OBS: observed concentrations, CMAQ (prior): modeled concentrations using the a priori NO_x emissions, CMAQ (posterior): modeled concentrations using the a posteriori NO_x emissions. Arrows indicate the changes in metrics from the prior model to the posterior model. R: Pearson's correlation coefficient, IOA: Index of Agreement, NMB: normalized mean bias (%), MAE: mean absolute error (ppb).

360 **Table 1:** Descriptive statistics comparing observed and modeled hourly surface NO_2 concentrations at ground-based measurement sites within each of the five source apportionment regions across East Asia during the period from January to May 2022. Prior: modeled concentrations using the a priori NO_x emissions, Posterior: modeled concentrations using the a posteriori NO_x emissions. R: Pearson's correlation coefficient, IOA: Index of Agreement, NMB: normalized mean bias (%), MAE: mean absolute error (ppb).

			January	February	March	April	May	5-month
Korea	Prior	R	0.89	0.88	0.63	0.73	0.82	0.67
		IOA	0.60	0.63	0.74	0.80	0.79	0.71
		NMB	-50.98	-48.58	-21.39	-20.64	-27.75	-32.75
		MAE	8.89	5.97	4.64	3.43	3.04	4.80
	Posterior	R	0.55	0.80	0.64	0.71	0.77	0.71
		IOA	0.71	0.85	0.79	0.83	0.82	0.82
		NMB	-17.37	-22.14	-4.17	-6.15	-18.84	-13.01
		MAE	5.85	3.65	4.02	2.93	2.39	3.56
Northeast China	Prior	R	0.59	0.51	0.72	0.41	0.26	0.39
		IOA	0.46	0.55	0.69	0.63	0.52	0.56
		NMB	-62.23	-50.37	-39.57	-18.70	-17.10	-39.06
		MAE	11.64	6.46	4.40	4.01	3.65	5.53
	Posterior	R	0.56	0.56	0.72	0.38	0.23	0.66
		IOA	0.73	0.72	0.79	0.63	0.51	0.80
		NMB	-1.57	1.15	-25.94	-10.67	-12.35	-9.40
		MAE	5.67	5.16	3.58	4.03	3.91	4.33
North China	Prior	R	0.67	0.61	0.75	0.66	0.69	0.68
		IOA	0.79	0.78	0.84	0.72	0.76	0.79
		NMB	-11.37	-3.15	-2.49	10.93	-8.03	-2.78
		MAE	5.28	5.27	4.53	5.27	4.18	4.85
	Posterior	R	0.58	0.63	0.78	0.72	0.80	0.73
		IOA	0.74	0.79	0.86	0.78	0.86	0.83
		NMB	-0.33	-1.47	6.64	15.33	-7.91	2.76
		MAE	5.82	4.72	4.28	4.40	3.04	4.30
East China	Prior	R	0.62	0.49	0.60	0.67	0.63	0.57
		IOA	0.67	0.69	0.74	0.75	0.77	0.74
		NMB	-27.63	-13.79	-13.88	-1.71	8.38	-9.65
		MAE	5.41	4.33	4.77	3.76	3.69	4.28
	Posterior	R	0.58	0.68	0.71	0.78	0.71	0.69
		IOA	0.73	0.81	0.81	0.81	0.82	0.82
		NMB	-16.19	-8.86	-0.55	4.00	3.67	-3.32
		MAE	4.29	3.41	3.93	3.46	3.23	3.61
South Central China	Prior	R	0.65	0.48	0.51	0.64	0.63	0.55
		IOA	0.73	0.69	0.67	0.71	0.74	0.72
		NMB	-23.43	-12.04	-16.33	-13.00	1.79	-12.41
		MAE	4.25	4.04	5.64	4.32	3.61	4.35
	Posterior	R	0.63	0.57	0.57	0.72	0.68	0.64
		IOA	0.77	0.75	0.71	0.76	0.78	0.77
		NMB	-12.17	-9.84	-14.60	-12.83	-4.75	-10.92
		MAE	3.90	3.68	5.16	3.91	3.38	3.99
China	Prior	R	0.72	0.61	0.68	0.69	0.68	0.65

(Northeast, North, East, and South Central)		IOA	0.73	0.76	0.80	0.76	0.80	0.79
		NMB	-25.65	-13.50	-12.79	-2.00	2.16	-10.26
		MAE	4.72	3.81	4.14	3.58	3.09	3.78
	Posterior	R	0.67	0.73	0.77	0.78	0.76	0.76
		IOA	0.81	0.85	0.86	0.83	0.85	0.86
		NMB	-8.44	-5.13	-3.20	2.26	-1.15	-3.04
		MAE	3.67	3.08	3.35	2.93	2.62	3.07

365

3.2 Source apportionment

Upon improving model accuracy, we assessed the contributions of NO_x emissions from local and outside sources to total NO_y concentrations in each of the five regions of East Asia during the winter-spring transition. NO_y concentrations were generally higher near the source regions throughout the months, with notable transboundary transport extending to downwind regions (Fig. 4). While local contributions remained substantial across all regions, a clear decreasing trend was seen as the season progressed. Local sources' contributions were greater during the winter months compared to those from transboundary sources, whereas spring months (March, April, and May) showed a marked increase in transboundary contributions across the regions (Fig. 4; Table 2). In January, local contributions were 31.50%, 42.62%, 37.42%, 33.69%, and 31.79% in Korea, Northeast China, North China, East China, and South Central China, respectively. By May, these decreased to 23.24%, 26.29%, 25.28%, 29.05%, and 30.06%. Meanwhile, transboundary contributions steadily increased as the months progressed. In January, transboundary contributions were 27.16%, 16.17%, 16.79%, 30.46%, and 33.39% in Korea, Northeast China, North China, East China, and South Central China, respectively. By May, these increased to 36.89%, 32.46%, 27.64%, 35.57%, and 35.70%. The decreases in local contributions can be partially attributed to reduced energy use and subsequent decline in anthropogenic emissions as the seasons transitioned to warmer months. However, this does not fully explain the concurrent increase in transboundary contributions, suggesting that NO_y concentrations from the sources did not readily remain near their origins but instead dispersed elsewhere, as reflected in the increasing transboundary contributions. However, this does not fully explain the concurrent increase in transboundary contributions, suggesting that other factors, such as the weakening of meteorological barriers, facilitated broader dispersion of NO_y from source regions. These dynamics are discussed further below.

%Source contributions to total NO$_y$ concentrations across East Asia
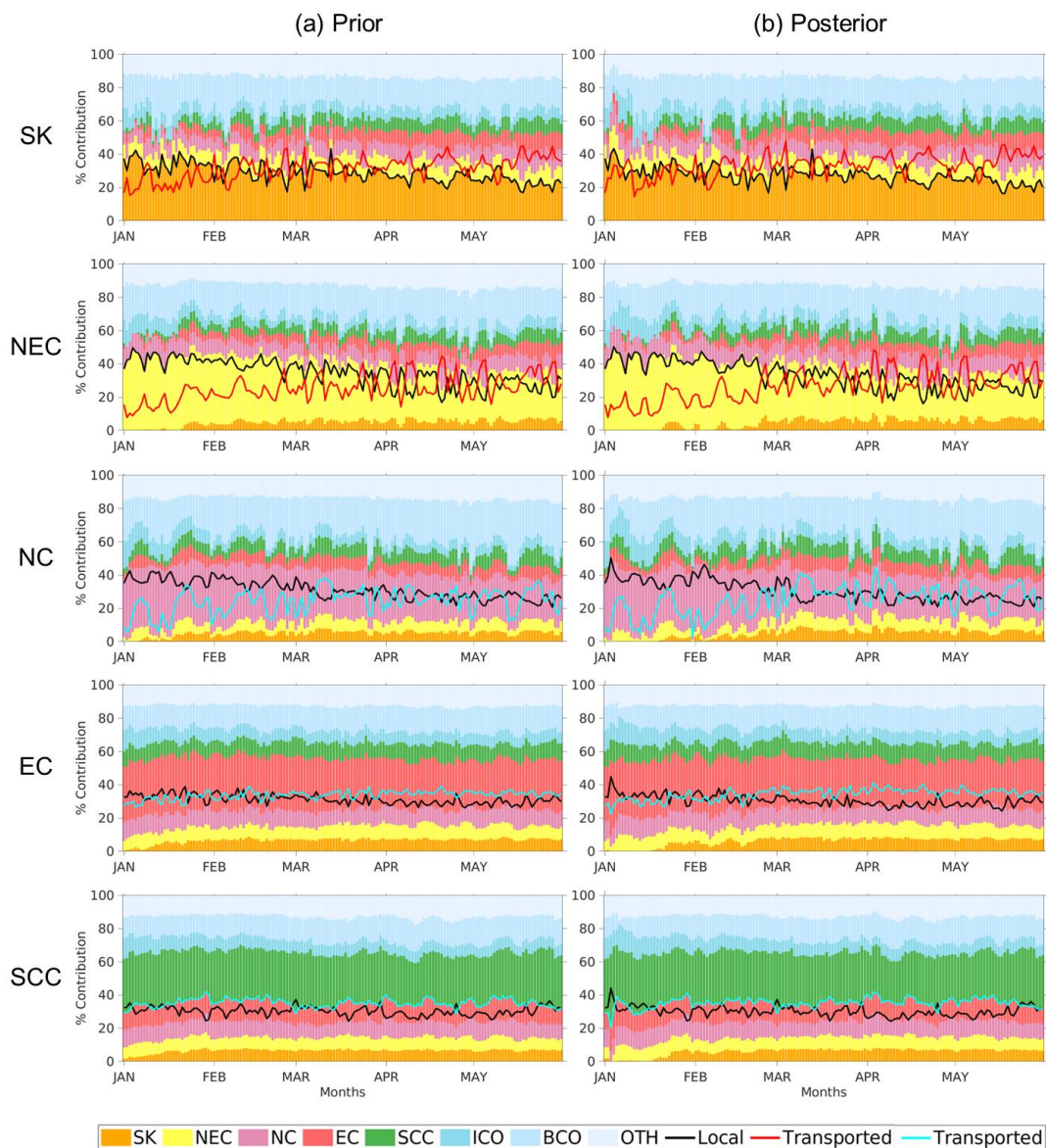
Figure 4: Percent contributions (%) of local and transboundary NO$_x$ emissions to NO$_y$ concentrations within the PBL in five source apportionment regions across East Asia during the period from January to May 2022. Prior and Posterior: percent contributions quantified based on the simulations using the a priori and a posteriori NO$_x$ emissions, respectively. ICO and BCO indicate the contributions from initial conditions and lateral boundary conditions, respectively, and OTH indicates the contribution of the emissions from the regions unspecified during ISAM.

Table 2: Descriptive statistics comparing the percent contributions (%) of local and transboundary NO_x emissions to NO_y concentrations within the PBL in five source apportionment regions across East Asia during the period from January to May 2022. Prior and Posterior: percent contributions quantified based on the simulations using the a priori and a posteriori NO_x emissions, respectively.

Receptor	Source	Model	January	February	March	April	May	Average
Korea	Korea (Local)	Prior	34.54	29.54	29.33	26.23	23.76	28.68
		Posterior	31.50	27.36	28.71	25.46	23.24	27.25
	Northeast China	Prior	8.34	8.84	9.18	9.14	8.96	8.89
		Posterior	9.77	9.28	9.49	9.48	9.23	9.45
	North China	Prior	8.27	9.03	8.62	9.03	9.89	8.97
		Posterior	9.63	9.93	9.11	9.41	10.25	9.67
	East China	Prior	3.52	6.36	8.02	8.89	9.79	7.32
		Posterior	4.48	5.57	8.36	9.10	9.88	7.48
	South Central China	Prior	3.20	5.94	6.82	7.44	7.32	6.15
		Posterior	3.28	6.85	7.34	7.89	7.53	6.58
	(Transboundary total)	Prior	23.33	30.17	32.64	34.50	35.97	31.32
		Posterior	27.16	31.63	34.31	35.88	36.89	33.17
Northeast China	Northeast China (Local)	Prior	43.21	39.70	34.99	28.26	27.49	34.73
		Posterior	42.62	38.93	32.97	26.86	26.29	33.53
	Korea	Prior	1.51	4.95	5.66	5.63	6.23	4.80
		Posterior	1.07	2.72	6.39	6.43	6.73	4.67
	North China	Prior	9.75	8.46	8.58	9.62	9.80	9.24
		Posterior	10.61	9.53	9.23	10.33	10.30	10.00
	East China	Prior	3.08	5.30	6.31	7.51	7.89	6.02
		Posterior	2.45	4.00	6.93	8.00	8.23	5.92
	South Central China	Prior	3.10	5.32	5.79	6.29	6.76	5.45
		Posterior	2.04	6.01	6.56	6.98	7.20	5.76
	(Transboundary total)	Prior	17.43	24.04	26.35	29.05	30.68	25.51
		Posterior	16.17	22.25	29.11	31.73	32.46	26.35
North China	North China (Local)	Prior	37.36	35.34	30.36	27.30	25.83	31.24
		Posterior	37.42	35.38	29.00	26.12	25.28	30.64
	Korea	Prior	2.68	5.16	5.94	5.60	5.58	4.99
		Posterior	0.86	3.71	6.78	6.60	6.11	4.81
	Northeast China	Prior	5.12	5.44	6.78	6.60	6.33	6.06
		Posterior	4.96	4.39	7.41	7.40	6.80	6.19
	East China	Prior	5.45	5.92	7.09	6.69	6.56	6.34
		Posterior	5.41	5.03	7.69	7.45	6.96	6.51
	South Central China	Prior	5.69	6.32	7.39	7.16	7.40	6.79
		Posterior	5.55	7.57	7.99	7.84	7.77	7.34
	(Transboundary total)	Prior	18.94	22.84	27.21	26.05	25.87	24.18
		Posterior	16.79	20.69	29.87	29.29	27.64	24.86
East China	East China (Local)	Prior	33.66	32.74	31.15	28.91	29.71	31.24
		Posterior	33.69	32.07	30.06	27.97	29.05	30.57
	Korea	Prior	4.21	7.09	7.20	7.23	7.27	6.60
		Posterior	1.83	5.82	7.76	7.68	7.48	6.11
	Northeast China	Prior	7.92	7.62	8.36	8.87	7.86	8.13
		Posterior	8.32	7.48	8.79	9.17	8.06	8.36
	North China	Prior	10.34	10.22	9.26	9.49	10.20	9.90
		Posterior	10.76	10.62	9.64	9.85	10.55	10.29
	South Central China	Prior	8.69	8.59	9.36	9.77	9.35	9.15
		Posterior	9.55	9.23	9.69	9.98	9.48	9.59

	(Transboundary total)	Prior	31.16	33.52	34.17	35.35	34.68	33.78
		Posterior	30.46	33.15	35.88	36.68	35.57	34.35
South Central China	Southeast China (Local)	Prior	31.22	30.52	30.89	28.23	30.40	30.25
		Posterior	31.79	30.53	30.48	27.83	30.06	30.14
	Korea	Prior	5.10	7.06	6.92	6.79	6.70	6.51
		Posterior	2.36	6.21	7.16	7.23	6.92	5.98
	Northeast China	Prior	7.87	7.31	7.57	7.87	7.19	7.56
		Posterior	7.99	7.19	7.76	8.19	7.38	7.70
	North China	Prior	10.16	10.08	8.87	9.39	9.76	9.65
		Posterior	10.54	10.32	9.08	9.77	10.05	9.95
	East China	Prior	11.84	12.30	10.65	11.10	11.43	11.46
		Posterior	12.49	12.15	10.71	11.16	11.34	11.57
	(Transboundary total)	Prior	34.97	36.74	34.01	35.15	35.09	35.19
		Posterior	33.39	35.87	34.71	36.34	35.70	35.20

395

The direction, reach, and amount of NO_y transport varied noticeably from January to May, driven by seasonal synoptic settings that influenced prevailing winds. During the winter months, NO_y transport was predominantly directed southeastward and eastward, seemingly consistent with the influence of the Siberian High, as shown by the presence of continental anticyclonic winds (Fig. 5). This explains the relatively small transboundary contributions in upwind Northeast China and North China during this period (Table 2). Such transport pattern was more pronounced when using the a posteriori NO_x emissions, showing an overall increase in transboundary NO_y transport (Fig. 5). After inversion, there was a noticeable increase in the amount of NO_y traveling from the source regions towards the southeast and east, reaffirming the typical wintertime pollution transport patterns. During the spring months (March, April, and May) (Fig. 6), the reach of NO_y transport expanded westward noticeably, allowing pollutants to travel more freely across a broader range of directions, rather than being confined to the dominant southeastward flow seen in winter. This can be attributed to the weakening of the Siberian High and the associated northwesterly winds, which enabled a more dynamic and multidirectional transport of pollutants across the regions. In addition, the emergence of seasonal easterlies during this time can facilitate occasional westward transport of pollutants, especially when a low-pressure system travels from west to east across the region, passing to the south of the weakening Siberian High (Peterson et al., 2019). This pattern was particularly evident when using the a posteriori NO_x emissions, as a broader reach of NO_y transport was shown in all directions, with greater pollutant dispersal across the regions.

In addition, when using the a priori and a posteriori NO_x emissions during spring, the severity of NO_y pollution did not necessarily decrease as the distance from each source region increased, shown by some NO_y hotspots far outside the sources (Fig. 6). For example, when the SMA was the source region, we noticed some high NO_y concentrations in highly populated regions in China such as Beijing, the Yangtze River Delta and Guangdong regions of China. Considering the "cooking time" allowed for NO_x to become NO_y components, which involves chemical reactions and transformations from NO_x to longer-lived species such as HNO_3 and PAN (Shimadera et al., 2014; Yuan et al., 2018; Sun et al., 2020; Kashfi Yeganeh, 2024), we concluded that the high NO_y loadings, particularly along the transport pathways, are secondary hotspots (Figs. S2 and S3);

the formations of such species depend on the availability of radicals and other precursors that are often more abundant in
420 urban environments, which emerged as these hotspots.

This expansion of transboundary contributions during the winter-spring transition reaffirms the critical role of seasonal dynamics in governing pollutant transport and dispersion, leading to increasingly complex cross-regional interactions. While some regions maintained consistent extents of transboundary contributions, others exhibited substantial fluctuations as the months progressed. For example, despite significant NO_x emissions (Fig. S2), Korea was initially the least influential source
425 region, contributing approximately from 1% to 5% to transboundary NO_y concentrations in neighboring regions during January due to the location relative to the dominant northwesterly. However, as the season transitioned, Korea's contribution to other regions grew, reaching up to 6%–7% by May, a notable increase comparable to the transboundary contributions shown by other regions (Table 2). Meanwhile, North China consistently emerged as the most influential source region, contributing around 10% to the NO_y concentrations of neighboring regions throughout the months. Besides North China's
430 dominance, East China and South Central China emerged as significant contributors to each other's NO_y budget, reflecting a close transboundary relationship between these regions. In addition, South Central China consistently experienced substantial transboundary contributions that outweighed local contributions by around 5% throughout the entire study period, indicating the region's vulnerability to pollution transport. Even though the winter months offer meteorological conditions more favorable for the directional transport of pollutants, transboundary contributions to NO_y loadings across the regions in
435 this season were generally smaller compared to spring. This can be attributed to the stronger winds typical of winter, which can facilitate rapid transport of pollutants, but also can drive them to pass through receptor regions more quickly, limiting their accumulation (Wang et al., 2023). In contrast, during the spring months, the weakening of northwesterly winds seemed to allow for broader pollutant transport in a more multidirectional manner, leading to increased transboundary mixing of pollutants.

440

Source contributions to total NO$_y$ concentrations across Asia: Winter 2022
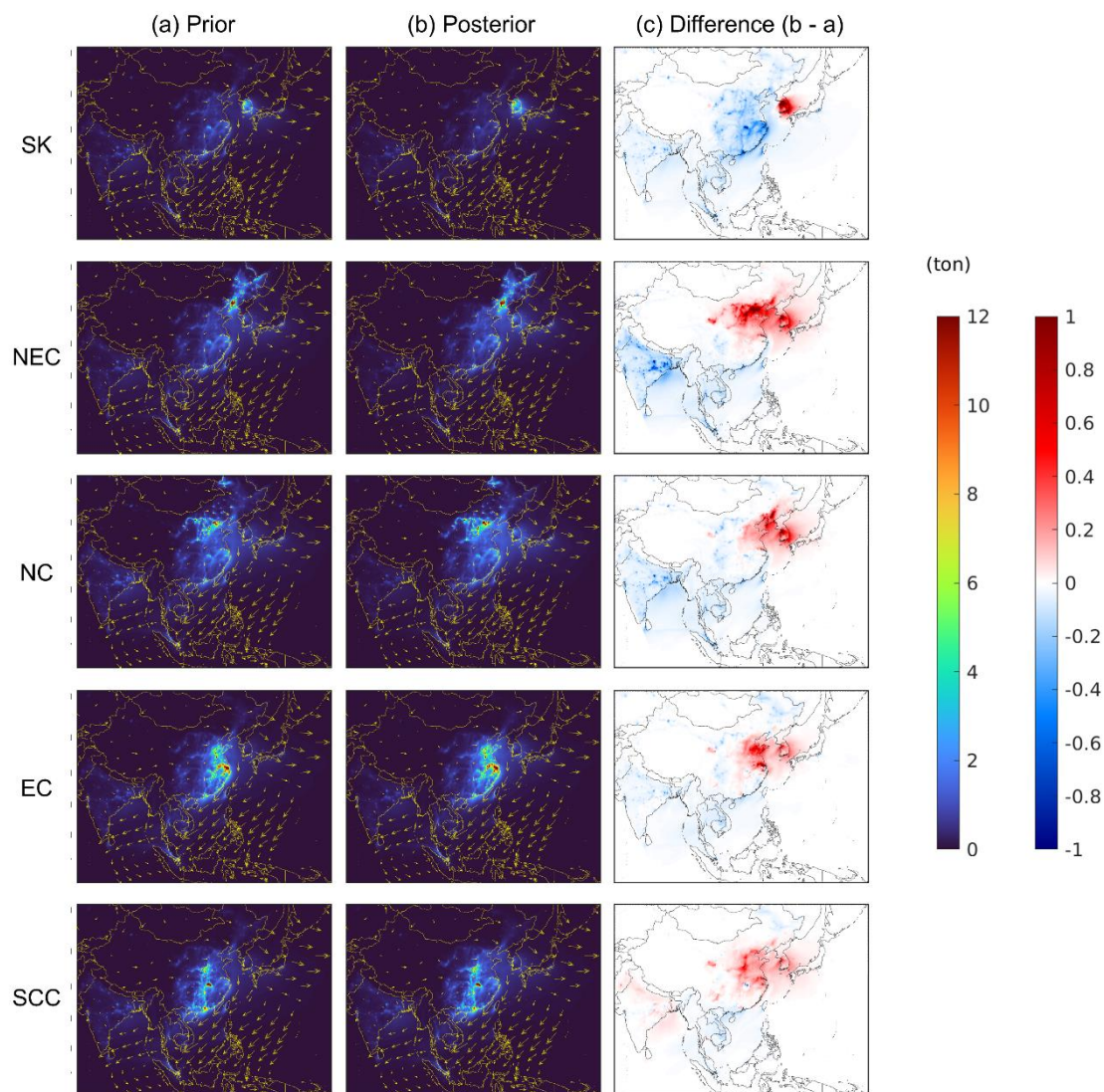
Figure 5: Source contributions to wintertime NO$_y$ concentrations (ton) within the PBL across Asia accumulated during the period from January to February 2022. (a) contributions quantified based on the simulations using the a priori NO$_x$ emissions, (b) contributions quantified based on the simulations using the a posteriori NO$_x$ emissions, (c) differences (b - a).

445

Source contributions to total NO$_y$ concentrations across Asia: Spring 2022
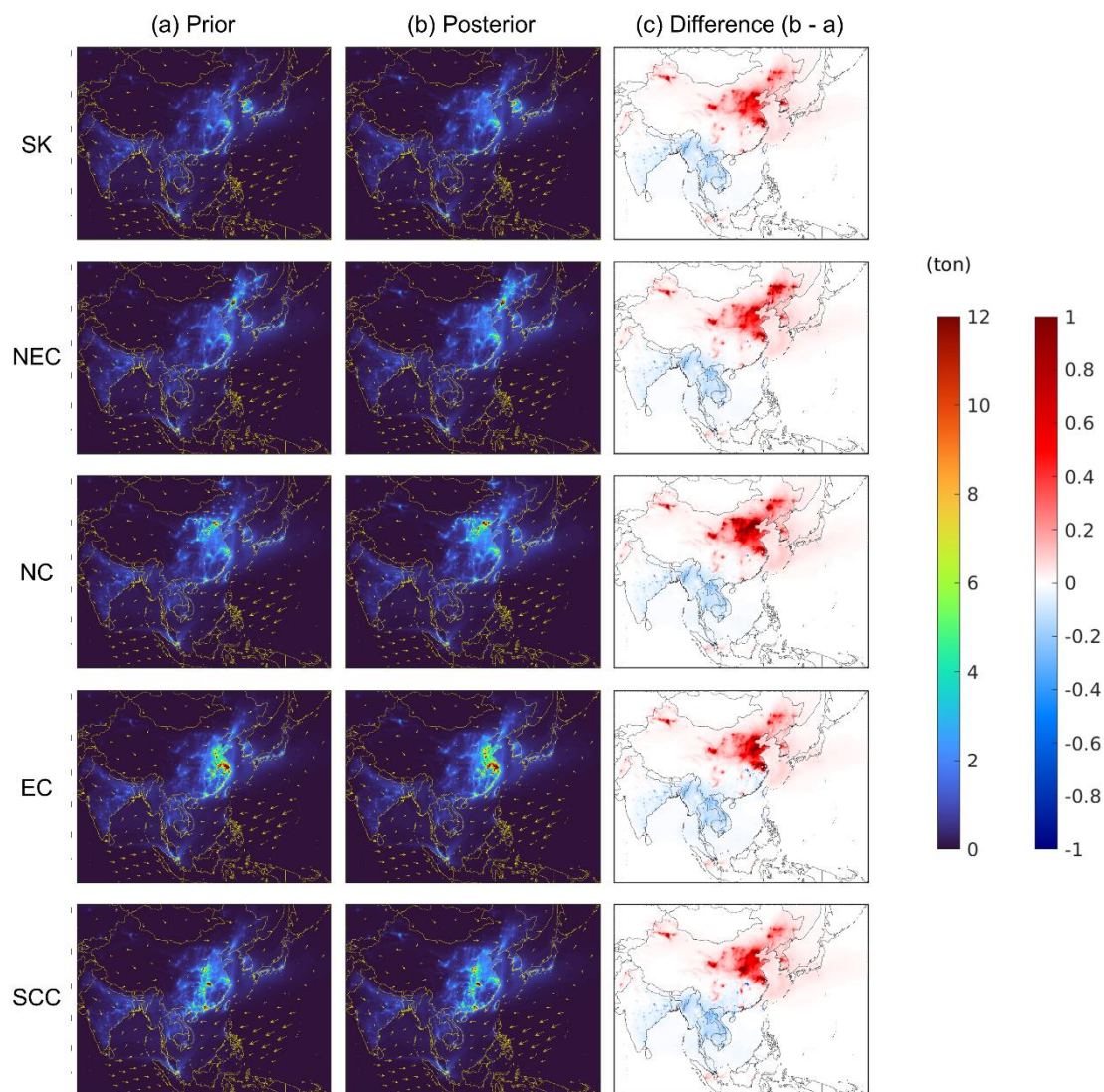
Figure 6: Source contributions to springtime NO$_y$ concentrations (ton) within the PBL across Asia accumulated during the period from March to May 2022. (a) contributions quantified based on the simulations using the a priori NO$_x$ emissions, (b) contributions quantified based on the simulations using the a posteriori NO$_x$ emissions, (c) differences (b - a).

3.3 Implications for PM$_{2.5}$ concentrations

While our study primarily focused on NO$_y$ loadings, the updates to the inventoried extent of NO$_x$ emissions also affected surface PM$_{2.5}$ concentrations across East Asia. While the posterior model generally underestimated PM$_{2.5}$ concentrations in
455   Korea and China, the overall increases in NO$_x$ emissions after the inversion led to corresponding increases in PM$_{2.5}$ concentrations, which improved model accuracy to a certain extent in the regions (Fig. 7; Table S3). In Korea, the use of the a posteriori NO$_x$ emissions reduced the extent of model underestimation in PM$_{2.5}$ concentrations from -21.01% to -16.95% on average during the winter-spring transition, leading to a slight improvement in IOA from 0.86 to 0.88, indicating better alignment between modeled and observed concentrations in the region. The improvement was less pronounced in China,
460   where the model underestimation was only slightly reduced from -32.50% to -31.05%, with minor increases in R from 0.61 to 0.64 and IOA from 0.60 to 0.62. In both Korea and China, the increases in PM$_{2.5}$ concentrations seemed to be responsive to the concurrent increases in nitrate aerosol concentrations, a major component of PM$_{2.5}$. For instance, our previous study across East Asia (Park et al., 2023) suggested that secondary inorganic aerosols, such as nitrate, sulfate, and ammonium, contributed around 53% of total PM$_{2.5}$ loadings in Korea, with nitrate aerosols alone accounting for 21%, on average during
465   the year 2019, while primary particulate matter made up around 47%. The improvements in our model accuracy suggest that the overall upward adjustments to NO$_x$ emissions, which likely promoted nitrate aerosol formation, helped remedy the model's prior underestimation of PM$_{2.5}$ concentrations. However, the underestimation still persisted after the inversion, particularly in China, suggesting a possible underrepresentation of other PM$_{2.5}$ precursor emissions beyond NO$_x$, such as sulfur dioxide (SO$_2$) and ammonia (NH$_3$), which were outside the scope of our study. Nonetheless, the response of PM$_{2.5}$
470   concentrations to the adjustments in NO$_x$ emissions reaffirmed the substantial contribution of secondary aerosols, such as nitrate, to regional PM$_{2.5}$ concentrations across East Asia.
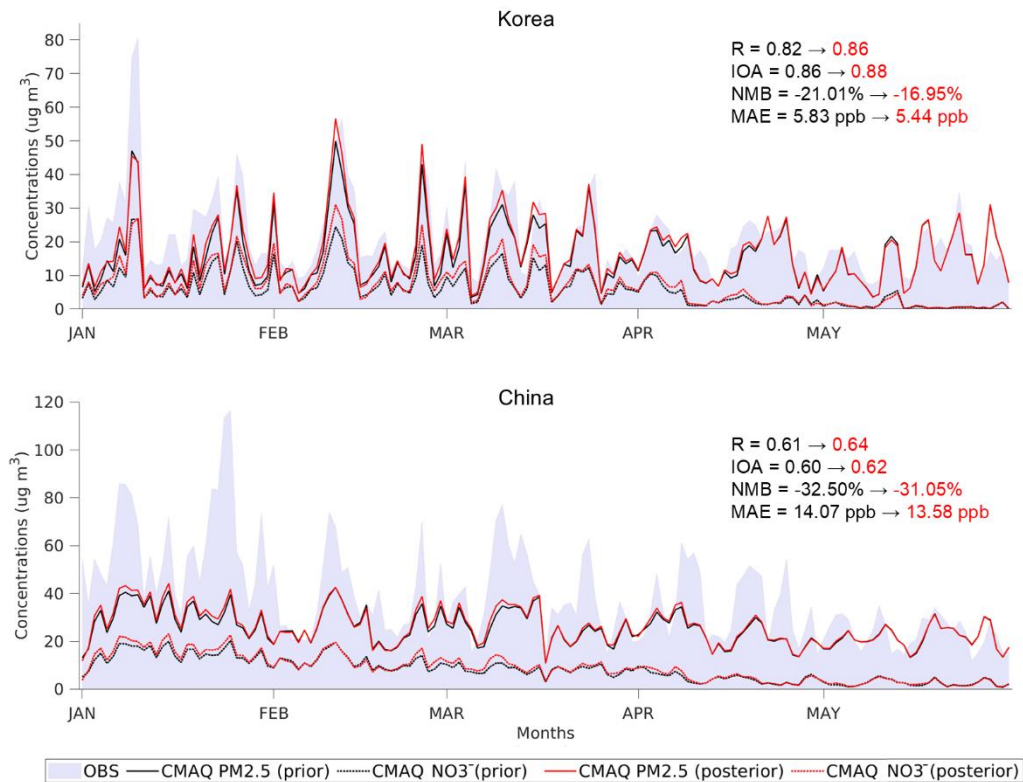
Figure 7: Daytime mean surface PM$_{2.5}$ concentrations observed and modeled at ground-based measurement sites during the period from January 1 to May 31, 2022. OBS: observed concentrations, CMAQ PM$_{2.5}$ (prior and posterior): modeled PM$_{2.5}$ concentrations using the a priori and a posteriori NO$_x$ emissions, CMAQ NO$_3^-$(prior and posterior): modeled nitrate aerosol (within PM$_{2.5}$ diameter) concentrations using the a priori and posteriori NO$_x$ emissions. Arrows indicate the changes in metrics from the prior model to the posterior model. R: Pearson's correlation coefficient, IOA: Index of Agreement, NMB: normalized mean bias (%), MAE: mean absolute error (ppb).

4 Conclusions

Our source apportionment effort, based on refined simulation accuracy, provided seasonal snapshots of NO_y transport across East Asia during the 2022 winter-spring transition. Our diurnal updates to the NO_x emission inventory led to overall increases in NO_x emissions in Korea and China by 50% and 33%, respectively. This suggests that the a priori estimates of NO_x emissions from the global dataset might have underrepresented emissions patterns to a certain extent, demanding follow-up efforts to better account for local emissions in a more nuanced manner. These increases in the inventoried amount of NO_x emissions substantially reduced the extent of the prior model's underestimation of surface NO_2 concentrations from -32.75% to -13.01% in Korea and from -10.26% to -3.04% in China, underscoring the utility of GEMS data as top-down constraints.

Leveraging the refined simulations, we quantified the local and transboundary contributions of NO_x emissions to East Asia's NO_y loadings during the winter-spring transition, focusing on our source apportionment regions including North China, Northeast China, East China, South Central China, and Korea. By comparing how much each region's NO_x emissions contributed to its own NO_y budget versus neighboring regions under seasonally varying synoptic settings, we assessed the cross-regional pollution transport dynamics and gained insights into source-receptor relationships across major NO_x-emitting regions of East Asia. During the winter months, pollutant transport was primarily influenced by strong northwesterly winds driven by the Siberian High, leading to significant transboundary contributions from upwind to downwind areas. As the Siberian High weakened in spring, transport patterns became more multidirectional, allowing pollutants to disperse farther across the regions. This seasonal transition resulted in increased transboundary contributions by up to 16% as the months progressed, as pollutants spread more extensively across the regions and potentially remained for an extended time near the receptors. From January to May, local contributions steadily decreased from 32%-43% to 23%-30%, while transboundary contributions showed an increasing trend from 16%-33% to 27%-37%. Some regions maintained their consistent contributions to East Asia's NO_y loadings, whereas others showed noticeable fluctuations in the contributions as the months progressed. North China consistently contributed over 10% to other regions' NO_y concentrations throughout the seasons, while Korea's contribution gradually increased from 1%-4% to 6%-7%, highlighting the critical role of seasonal synoptic conditions in governing pollution transport. This shift illustrates how a once less influential source region can become a significant contributor as seasons progress. While East China and South Central China substantially contributed to each other's NO_y budget by 9%-12%, South Central China consistently experienced transboundary impacts that consistently exceeded its local contribution by 5%, indicating its vulnerability to pollution transport. These findings highlight the complexity of seasonal pollution dynamics and the evolving nature of transboundary impacts, underscoring the need for adaptive air quality management strategies that account for shifting transport patterns between emission sources and receptor regions.

A limitation of our study is that the source apportionment was largely confined to East Asia, despite our simulation domain covering the entirety of Asia. This limitation was primarily due to our study's objective, which necessitated improving model accuracy through indirect evaluation of the a posteriori emission inventory's reliability, comparing modeled surface NO_2 concentrations against station measurements, which were available only for Korea and China during the study period. The absence of ground-based measurements from other regions in Asia during this period restricted the validation of the model's performance outside East Asia, limiting the broader applicability of our findings. Nonetheless, our study provides a comprehensive perspective on NO_y transport dynamics, addressing the broader geographic context and extended simulation period that demand a more rigorous investigation. Future studies could build upon this approach by extending the study period to cover additional seasons, such as summer and fall, to capture year-round pollution transport dynamics. A long-term, decadal study could reveal evolving trends in transboundary pollution, particularly during the winter-spring transition, and provide deeper insights into how policy changes, economic developments, and climate variations shape pollution patterns over time. These follow-up investigations would offer a more comprehensive understanding of East Asia's air quality challenges and further support the development of adaptive, long-term strategies for managing transboundary air pollution.

Acknowledgments

This work was partially supported by a grant from the National Institute of Environment Research (NIER), funded by the Ministry of Environment (MOE) of the Republic of Korea (NIER-2023-04-02-082). We thank the Research Computing Data Core at University of Houston for providing the supercomputing resources that supported this work.

Data availability

GEMS Level 2 products are available through Open-API at https://nesc.nier.go.kr/ko/html/svc/openapi/explain.do (in Korean) (last accessed on October 16, 2024), managed by the NIER's Environmental Satellite Center. Quality-assured AirKorea measurement datasets are available on the AirKorea website at https://www.airkorea.or.kr/web/last_amb_hour_data?pMENU_NO=123 (in Korean) (last accessed on October 16, 2024). MEE measurement datasets are available on the online archive at https://quotsoft.net/air/ (in Chinese) (last accessed on April 11, 2024), originally sourced from the China National Environmental Monitoring Center (CNEMC) database.

Author contribution

JP took the lead in drafting the original manuscript. JP and YC set up the experimental design. JP set up the models and conducted air quality simulations. JP and SK performed top-down adjustments to the emission inventory. JP conducted source apportionment. JP, YC, and SK evaluated the emissions adjustment and source apportionment outcomes. YC

540   provided overall context as a principal investigator and supervised the entire research. All authors discussed the results and exchanged feedback to prepare the final version of the manuscript draft.

Competing interests

The authors declare that they have no conflict of interest.

References

Bae, C., Kim, B.-U., Kim, H. C., Yoo, C., and Kim, S.: Long-range transport influence on key chemical components of PM$_{2.5}$ in the Seoul Metropolitan Area, South Korea, during the years 2012–2016. Atmosphere-BaseL, 11(1), Article 1. https://doi.org/10.3390/atmos11010048, 2020.

Beirle, S., Boersma, K. F., Platt, U., Lawrence, M. G., and Wagner, T.: Megacity emissions and lifetimes of nitrogen oxides probed from space, Science, 333(6050), 1737–1739, 2011.

Byun, D., and Schere, K. L.: Review of the governing equations, computational algorithms, and other components of the Models-3 Community Multiscale Air Quality (CMAQ) modeling system, Appl. Mech. Rev., 59(2), 51–77, https://doi.org/10.1115/1.2128636, 2006.

Carmichael, G. R., Calori, G., Hayami, H., Uno, I., Cho, S. Y., Engardt, M., Kim, S.-B., Ichikawa, Y., Ikeda, Y., Woo, J.-H., Ueda, H., and Amann, M.: The MICS-Asia study: Model intercomparison of long-range transport and sulfur deposition in East Asia, Atmos. Environ., 36(2), 175–199, https://doi.org/10.1016/S1352-2310(01)00448-4, 2002.

Chen, D., Xia, L., Guo, X., Lang, J., Zhou, Y., Wei, L., and Fu, X.: Impact of inter-annual meteorological variation from 2001 to 2015 on the contribution of regional transport to PM$_{2.5}$ in Beijing, China, Atmos. Environ., 260, 118545, https://doi.org/10.1016/j.atmosenv.2021.118545, 2021.

Choi, W. J., Moon, K.-J., Yoon, J., Cho, A., Kim, S., Lee, S., Ko, D. ho, Kim, J., Ahn, M. H., Kim, D.-R., Kim, S.-M., Kim, J.-Y., Nicks, D., and Kim, J.-S.: Introducing the geostationary environment monitoring spectrometer, J. Appl. Remote. Sens., 12(4), 044005, https://doi.org/10.1117/1.JRS.12.044005, 2018.

Clough, S. A., Shephard, M. W., Mlawer, E. J., Delamere, J. S., Iacono, M. J., Cady-Pereira, K., Boukabara, S., and Brown, P. D.: Atmospheric radiative transfer modeling: A summary of the AER codes, J. Quant. Spectrosc. Ra., 91(2), 233–244, https://doi.org/10.1016/j.jqsrt.2004.05.058, 2005.

Collet, S., Kidokoro, T., Karamchandani, P., Jung, J., and Shah, T.: Future year ozone source attribution modeling study using CMAQ-ISAM. J. Air. Waste. Manage., 68(11), 1239–1247, https://doi.org/10.1080/10962247.2018.1496954, 2018.

Crippa, M., Solazzo, E., Huang, G., Guizzardi, D., Koffi, E., Muntean, M., Schieberle, C., Friedrich, R., and Janssens-Maenhout, G.: High resolution temporal profiles in the Emissions Database for Global Atmospheric Research. Sci. Data, 7(1), Article 1, https://doi.org/10.1038/s41597-020-0462-2, 2020.

Dong, Z., Wang, S., Xing, J., Chang, X., Ding, D., and Zheng, H.: Regional transport in Beijing-Tianjin-Hebei region and its changes during 2014–2017: The impacts of meteorology and emission reduction, Sci. Total Environ., 737, 139792, https://doi.org/10.1016/j.scitotenv.2020.139792, 2020.

Eck, T. F., Holben, B. N., Kim, J., Beyersdorf, A. J., Choi, M., Lee, S., Koo, J.-H., Giles, D. M., Schafer, J. S., Sinyuk, A., Peterson, D. A., Reid, J. S., Arola, A., Slutsker, I., Smirnov, A., Sorokin, M., Kraft, J., Crawford, J. H., Anderson, B. E., Thornhill, K. L., Diskin, G., Kim, S., Park, S.: Influence of cloud, fog, and high relative humidity during pollution

transport events in South Korea: Aerosol properties and PM$_{2.5}$ variability. Atmos. Environ., 232, 117530. https://doi.org/10.1016/j.atmosenv.2020.117530, 2020.

580 Feng, X., Zhang, X., and Wang, J.: Update of SO$_2$ emission inventory in the Megacity of Chongqing, China by inverse modeling. Atmos. Environ., 294, 119519, https://doi.org/10.1016/j.atmosenv.2022.119519, 2023.

Goldberg, D. L., Saide, P. E., Lamsal, L. N., de Foy, B., Lu, Z., Woo, J.-H., Kim, Y., Kim, J., Gao, M., Carmichael, G., and Streets, D. G.: A top-down assessment using OMI NO$_2$ suggests an underestimate in the NO$_x$ emissions inventory in Seoul, South Korea, during KORUS-AQ, Atmos. Chem. Phys., 19(3), 1801–1818. https://doi.org/10.5194/acp-19-
585 1801-2019, 2019.

Goldberg, D. L., Tao, M., Kerr, G. H., Ma, S., Tong, D. Q., Fiore, A. M., Dickens, A. F., Adelman, Z. E., and Anenberg, S. C.: Evaluating the spatial patterns of U.S. urban NO$_x$ emissions using TROPOMI NO$_2$. Remote. Sens. Environ., 300, 113917. https://doi.org/10.1016/j.rse.2023.113917, 2024.

Guenther, A.B., Karl, T., Harley, P., Wiedinmyer, C., Palmer, P. I., and Geron, C.: Estimates of global terrestrial isoprene
590 emissions using MEGAN (Model of Emissions of Gases and Aerosols from Nature), Atmos. Chem. and Phys., 6(11), 3181–3210, https://doi.org/10.5194/acp-6-3181-2006, 2006.

Guenther, A., Jiang, X., Shah, T., Huang, L., Kemball-Cook, S., and Yarwood, G.: Model of Emissions of Gases and Aerosol from Nature Version 3 (MEGAN3) for Estimating Biogenic Emissions, In C. Mensink, W. Gong, and A. Hakami (Eds.), Air Pollution Modeling and its Application XXVI, 187–192, Springer International Publishing,
595 https://doi.org/10.1007/978-3-030-22055-6_29, 2020.

Han, X., Cai, J., Zhang, M., and Wang, X.: Numerical simulation of interannual variation in transboundary contributions from Chinese emissions to PM$_{2.5}$ mass burden in South Korea, Atmospheric Environment, 256, 118440, https://doi.org/10.1016/j.atmosenv.2021.118440, 2021.

Hertel, O., Skjøth, C. A., Reis, S., Bleeker, A., Harrison, R. M., Cape, J. N., Fowler, D., Skiba, U., Simpson, D., Jickells, T.,
600 Kulmala, M., Gyldenkærne, S., Sørensen, L. L., Erisman, J. W., and Sutton, M. A.: Governing processes for reactive nitrogen compounds in the European atmosphere, Biogeosciences, 9(12), 4921–4954, https://doi.org/10.5194/bg-9-4921-2012, 2012.

Hoek, G., Krishnan, R. M., Beelen, R., Peters, A., Ostro, B., Brunekreef, B., and Kaufman, J. D.: Long-term air pollution exposure and cardio- respiratory mortality: A review, Environ. Health, 12(1), 43, https://doi.org/10.1186/1476-069X-
605 12-43, 2013.

Houyoux, M. R., Vukovich, J. M., Coats Jr., C. J., Wheeler, N. J. M., and Kasibhatla, P. S.: Emission inventory development and processing for the Seasonal Model for Regional Air Quality (SMRAQ) project, J. Geophys. Res-Atmos., 105(D7), 9079–9090, https://doi.org/10.1029/1999JD900975, 2000.

Hui, G.: Comparison of East Asian winter monsoon indices, Adv. Geosci., 10, 31–37, https://doi.org/10.5194/adgeo-10-31-
610 2007, 2007.

Iacono, M. J., Delamere, J. S., Mlawer, E. J., Shephard, M. W., Clough, S. A., and Collins, W. D.: Radiative forcing by long-lived greenhouse gases: Calculations with the AER radiative transfer models, J. Geophys. Res-atmos., 113(D13), https://doi.org/10.1029/2008JD009944, 2008.

Ikeda, K., Yamaji, K., Kanaya, Y., Taketani, F., Pan, X., Komazaki, Y., Kurokawa, J., and Ohara, T.: Source region attribution of $PM_{2.5}$ mass concentrations over Japan, Geochem. J., 49(2), 185–194, https://doi.org/10.2343/geochemj.2.0344, 2015.

Itahashi, S., Uno, I., and Kim, S.: Source contributions of sulfate aerosol over East Asia estimated by CMAQ-DDM, Environ. Sci. Technol., 46(12), 6733–6741, https://doi.org/10.1021/es300887w, 2012.

Jeon, W., Choi, Y., Lee, H. W., Lee, S.-H., Yoo, J.-W., Park, J., and Lee, H.-J.: A quantitative analysis of grid nudging effect on each process of $PM_{2.5}$ production in the Korean Peninsula, Atmos. Environ., 122, 763–774, https://doi.org/10.1016/j.atmosenv.2015.10.050, 2015.

Jiang, Z., Vargas, M., and Csiszar, I.: New operational real-time daily rolling weekly Green Vegetation fraction product derived from suomi NPP VIIRS reflectance data. 2016 IEEE International Geoscience and Remote Sensing Symposium (IGARSS), Beijing, China, 10-15 July 2016, 3524–3527, https://doi.org/10.1109/IGARSS.2016.7729911, 2016.

Jordan, C. E., Crawford, J. H., Beyersdorf, A. J., Eck, T. F., Halliday, H. S., Nault, B. A., Chang, L.-S., Park, J., Park, R., Lee, G., Kim, H., Ahn, J., Cho, S., Shin, H. J., Lee, J. H., Jung, J., Kim, D.-S., Lee, M., Lee, T., … Schwarz, J. P.: Investigation of factors controlling $PM_{2.5}$ variability across the South Korean Peninsula during KORUS-AQ. Elementa-Sci. Anthrop., 8, 28. https://doi.org/10.1525/elementa.424, 2020.

Jung, J., Choi, Y., Wong, D. C., Nelson, D., and Lee, S.: Role of Sea Fog Over the Yellow Sea on Air Quality With the Direct Effect of Aerosols. Journal of Geophysical Research: Atmospheres, 126(5), e2020JD033498. https://doi.org/10.1029/2020JD033498, 2021.

Jung, J., Choi, Y., Souri, A. H., Mousavinezhad, S., Sayeed, A., and Lee, K.: The impact of springtime-transported air pollutants on local air quality with satellite-constrained NO_x emission adjustments over East Asia, J. Geophy. Res-Atmos., 127(5), e2021JD035251, https://doi.org/10.1029/2021JD035251, 2022a.

Jung, J., Choi, Y., Mousavinezhad, S., Kang, D., Park, J., Pouyaei, A., Ghahremanloo, M., Momeni, M., and Kim, H.: Changes in the ozone chemical regime over the contiguous United States inferred by the inversion of NOx and VOC emissions using satellite observation. Atmospheric Research, 270, 106076. https://doi.org/10.1016/j.atmosres.2022.106076, 2022b.

Kain, J. S.: The Kain–Fritsch convective parameterization: An update, J. Appl. Meteorol. Clim., 43(1), 170–181, https://doi.org/10.1175/1520-0450(2004)043<0170:TKCPAU>2.0.CO;2, 2004.

Kajino, M., Sato, K., Inomata, Y., and Ueda, H.: Source–receptor relationships of nitrate in Northeast Asia and influence of sea salt on the long-range transport of nitrate, Atmos. Environ., 79, 67–78. https://doi.org/10.1016/j.atmosenv.2013.06.024, 2013.

Kang, M.-S., Park, D.-S., Chae, C.-B., Sunwoo, Y., and Hong, K.-H.: Monthly characteristics and source–receptor relationships of anthropogenic total nitrate in Northeast Asia, Atmosphere-BaseL, 15(9), Article 9. https://doi.org/10.3390/atmos15091121, 2024.

Kashfi Yeganeh, A., Momeni, M., Choi, Y., Park, J., and Jung, J.: A case study of surface ozone source contributions in the Seoul metropolitan area using the adjoint of CMAQ, Japca. J. Air. Waste. Ma, 74(7), 511–530, https://doi.org/10.1080/10962247.2024.2361021, 2024.

Kim, Y., Kim, K.-Y., and Jhun, J.-G.: Seasonal evolution mechanism of the East Asian winter monsoon and its interannual variability. Clim. Dynam., 41(5), 1213–1228, https://doi.org/10.1007/s00382-012-1491-0, 2013.

Lange, K., Richter, A., and Burrows, J. P.: Variability of nitrogen oxide emission fluxes and lifetimes estimated from Sentinel-5P TROPOMI observations. Atmos. Chem. Phys., 22(4), 2745–2767, https://doi.org/10.5194/acp-22-2745-2022, 2022.

Lee, H.-J., Jo, H.-Y., Song, C.-K., Jo, Y.-J., Park, S.-Y., and Kim, C.-H.: Sensitivity of simulated $PM_{2.5}$ concentrations over northeast Asia to different secondary organic aerosol modules during the KORUS-AQ campaign. Atmosphere-BaseL, 11(9), Article 9. https://doi.org/10.3390/atmos11091004, 2020.

Li, M., Liu, H., Geng, G., Hong, C., Liu, F., Song, Y., Tong, D., Zheng, B., Cui, H., Man, H., Zhang, Q., and He, K: Anthropogenic emission inventories in China: A review, Natl. Sci. Rev., 4(6), 834–866, https://doi.org/10.1093/nsr/nwx150, 2017a.

Li, Z., Guo, J., Ding, A., Liao, H., Liu, J., Sun, Y., Wang, T., Xue, H., Zhang, H., and Zhu, B.: Aerosol and boundary-layer interactions and impact on air quality, Natl. Sci. Rev., 4(6), 810–833, https://doi.org/10.1093/nsr/nwx117, 2017b.

Li, R., Mei, X., Wei, L., Han, X., Zhang, M., and Jing, Y.: Study on the contribution of transport to $PM_{2.5}$ in typical regions of China using the regional air quality model RAMS-CMAQ, Atmos. Environ., 214, 116856, https://doi.org/10.1016/j.atmosenv.2019.116856, 2019.

Li, M., McDonald, B. C., McKeen, S. A., Eskes, H., Levelt, P., Francoeur, C., Harkins, C., He, J., Barth, M., Henze, D. K., Bela, M. M., Trainer, M., de Gouw, J. A., and Frost, G. J.: Assessment of Updated Fuel-Based Emissions Inventories Over the Contiguous United States Using TROPOMI NO_2 Retrievals, J. Geophys. Res-Atmos., 126(24), e2021JD035484, https://doi.org/10.1029/2021JD035484, 2021a.

Li, N., Tang, K., Wang, Y., Wang, J., Feng, W., Zhang, H., Liao, H., Hu, J., Long, X., Shi, C., and Su, X.: Is the efficacy of satellite-based inversion of SO_2 emission model dependent?, Environ. Res. Lett., 16(3), 035018, https://doi.org/10.1088/1748-9326/abe829, 2021b.

Lin, J.-T., Liu, Z., Zhang, Q., Liu, H., Mao, J., and Zhuang, G.: Modeling uncertainties for tropospheric nitrogen dioxide columns affecting satellite-based inverse modeling of nitrogen oxides emissions, Atmos. Chem. and Phys., 12(24), 12255–12275, https://doi.org/10.5194/acp-12-12255-2012, 2012.

Liu, F., Beirle, S., Zhang, Q., Dörner, S., He, K., and Wagner, T.: NO$_x$ lifetimes and emissions of cities and power plants in polluted background estimated by satellite observations, Atmos. Chem. and Phys., 16(8), 5283–5298. https://doi.org/10.5194/acp-16-5283-2016, 2016.

Liu, B., Jin, Y., and Li, C. Analysis and prediction of air quality in Nanjing from autumn 2018 to summer 2019 using PCR–SVR–ARMA combined model, Sci. Rep-UK., 11(1), 348. https://doi.org/10.1038/s41598-020-79462-0, 2021.

Martin, R. V., Jacob, D. J., Chance, K., Kurosu, T. P., Palmer, P. I., and Evans, M. J.: Global inventory of nitrogen oxide emissions constrained by space-based observations of NO2 columns. Journal of Geophysical Research: Atmospheres, 108(D17). https://doi.org/10.1029/2003JD003453, 2003.

Momeni, M., Choi, Y., Kashfi Yeganeh, A., Pouyaei, A., Jung, J., Park, J., Shephard, M. W., Dammers, E., and Cady-Pereira, K. E.: Constraining East Asia ammonia emissions through satellite observations and iterative Finite Difference Mass Balance (iFDMB) and investigating its impact on inorganic fine particulate matter, Environ. Int., 184, 108473, https://doi.org/10.1016/j.envint.2024.108473, 2024.

Mun, J., Choi, Y., Jeon, W., Lee, H. W., Kim, C.-H., Park, S.-Y., Bak, J., Jung, J., Oh, I., Park, J., and Kim, D.: Assessing mass balance-based inverse modeling methods via a pseudo-observation test to constrain NO$_x$ emissions over South Korea, Atmos. Environ., 292, 119429, https://doi.org/10.1016/j.atmosenv.2022.119429, 2023.

Morrison, H., Thompson, G., and Tatarskii, V.: Impact of cloud microphysics on the development of trailing stratiform precipitation in a simulated squall line: Comparison of one- and two-moment schemes, Mon. Weather. Rev., 137(3), 991–1007, https://doi.org/10.1175/2008MWR2556.1, 2009.

Napelenok, S. L., Cohan, D. S., Hu, Y., and Russell, A. G.: Decoupled direct 3D sensitivity analysis for particulate matter (DDM-3D/PM). Atmos. Environ., 40(32), 6112–6121, https://doi.org/10.1016/j.atmosenv.2006.05.039, 2006.

Nault, B. A., Campuzano-Jost, P., Day, D. A., Schroder, J. C., Anderson, B., Beyersdorf, A. J., Blake, D. R., Brune, W. H., Choi, Y., Corr, C. A., de Gouw, J. A., Dibb, J., DiGangi, J. P., Diskin, G. S., Fried, A., Huey, L. G., Kim, M. J., Knote, C. J., Lamb, K. D., … Jimenez, J. L.: Secondary organic aerosol production from local emissions dominates the organic aerosol budget over Seoul, South Korea, during KORUS-AQ. Atmos. Chem. and Phys., 18(24), 17769–17800. https://doi.org/10.5194/acp-18-17769-2018, 2018.

Newell, K., Kartsonaki, C., Lam, K. B. H., and Kurmi, O.: Cardiorespiratory health effects of gaseous ambient air pollution exposure in low and middle income countries: A systematic review and meta-analysis, Environ. Health., 17(1), 41. https://doi.org/10.1186/s12940-018-0380-3, 2018.

Environmental Satellite Center, National Institute of Environmental Research (NIER), Korea Ministry of Environment: Geostationary Environment Monitoring Spectrometer (GEMS) algorithm theoretical basis document: NO$_2$ retrieval algorithm. Retrieved from https://nesc.nier.go.kr/en/html/satellite/doc/doc.do (last accessed Nov 30, 2024), 2020.

Pan, L., Tong, D., Lee, P., Kim, H.-C., and Chai, T.: Assessment of NO$_x$ and O$_3$ forecasting performances in the U.S. National Air Quality Forecasting Capability before and after the 2012 major emissions updates, Atmos. Environ., 95, 610–619. https://doi.org/10.1016/j.atmosenv.2014.06.020, 2014.

Park, J., and Lee, P. S.-H. Relationship between remotely sensed ambient PM_{10} and $PM_{2.5}$ and urban forest in Seoul, South Korea. Forests, 11(10), Article 10, https://doi.org/10.3390/f11101060, 2020.

Park, J., Jung, J., Choi, Y., Mousavinezhad, S., and Pouyaei, A.: The sensitivities of ozone and $PM_{2.5}$ concentrations to the satellite-derived leaf area index over East Asia and its neighboring seas in the WRF-CMAQ modeling system, Environ. Pollut., 306, 119419, https://doi.org/10.1016/j.envpol.2022.119419, 2022.

Park, J., Jung, J., Choi, Y., Lim, H., Kim, M., Lee, K., Lee, Y. G., and Kim, J. Satellite-based, top-down approach for the adjustment of aerosol precursor emissions over East Asia: The TROPOspheric Monitoring Instrument (TROPOMI) NO_2 product and the Geostationary Environment Monitoring Spectrometer (GEMS) aerosol optical depth (AOD) data fusion product and its proxy, Atmos. Meas. Tech., 16(12), 3039–3057, https://doi.org/10.5194/amt-16-3039-2023, 2023.

Park, J., Choi, Y., Jung, J., Lee, K., and Yeganeh, A. K.: First top-down diurnal adjustment to NO_x emissions inventory in Asia informed by the Geostationary Environment Monitoring Spectrometer (GEMS) tropospheric NO_2 columns, Sci. Rep-UK., 14(1), 24338. https://doi.org/10.1038/s41598-024-76223-1, 2024.

Peterson, D. A., Hyer, E. J., Han, S.-O., Crawford, J. H., Park, R. J., Holz, R., Kuehn, R. E., Eloranta, E., Knote, C., Jordan, C. E., and Lefer, B. L.: Meteorology influencing springtime air quality, pollution transport, and visibility in Korea, Elementa, 7, 57, https://doi.org/10.1525/elementa.395, 2019.

Placet, M., Mann, C. O., Gilbert, R. O., and Niefer, M. J., Emissions of ozone precursors from stationary sources: A critical review, Atmos. Environ., 34(12), 2183–2204, https://doi.org/10.1016/S1352-2310(99)00464-1, 2000.

Pleim, J. E., Xiu, A., Finkelstein, P. L., and Otte, T. L.: A coupled land-surface and dry deposition model and comparison to field measurements of surface heat, moisture, and ozone fluxes, Water. Air. Soil. Poll., 1(5), 243–252. https://doi.org/10.1023/A:1013123725860, 2001.

Pleim, J. E.: A simple, efficient solution of flux–profile relationships in the atmospheric surface layer. J. Appl. Meteorol. Clim., 45(2), 341–347, https://doi.org/10.1175/JAM2339.1, 2006.

Pleim, J. E.: A combined local and nonlocal closure model for the atmospheric boundary layer Part I: Model description and testing, J. Appl. Meteorol. Clim., 46(9), 1383–1395, https://doi.org/10.1175/JAM2539.1, 2007a.

Pleim, J. E.: A combined local and nonlocal closure model for the atmospheric boundary layer Part II: Application and evaluation in a mesoscale meteorological model, J. Appl. Meteorol. Clim., 46(9), 1396–1409, https://doi.org/10.1175/JAM2534.1, 2007b.

Rodgers, C. D.: Inverse methods for atmospheric sounding: Theory and practice, Series on Atmospheric, Oceanic and Planetary Physics, World Scientific, https://doi.org/10.1142/3171, 2000.

Rohde, R. A., and Muller, R. A.: Air pollution in China: Mapping of concentrations and sources. PLOS ONE, 10(8), e0135749, https://doi.org/10.1371/journal.pone.0135749, 2015.

Russo, M. A., Gama, C., and Monteiro, A.: How does upgrading an emissions inventory affect air quality simulations?, Air. Qual. Atmos. Hlth., 12(6), 731–741, https://doi.org/10.1007/s11869-019-00692-x, 2019.

Rypdal, K., and Winiwarter, W.: Uncertainties in greenhouse gas emission inventories—Evaluation, comparability and implications, Environ. Sci. Policy., 4(2), 107–116, https://doi.org/10.1016/S1462-9011(00)00113-1, 2001.

745 Ryu, Y.-H., and Min, S.-K.: Anthropogenic warming degrades spring air quality in Northeast Asia by enhancing atmospheric stability and transboundary transport, Npj. Clim. Atmos. Sci., 7(1), 1–10, https://doi.org/10.1038/s41612-024-00603-7, 2024.

Sargent, M. R., Floerchinger, C., McKain, K., Budney, J., Gottlieb, E. W., Hutyra, L. R., Rudek, J., and Wofsy, S. C.: Majority of US urban natural gas emissions unaccounted for in inventories, P. Natl. Acad. Sci., 118(44), e2105804118,
750 https://doi.org/10.1073/pnas.2105804118, 2021.

Shen, A., Liu, Y., Lu, X., Wang, X., Chang, M., Zhang, J., Tian, C., and Fan, Q.: Sulfur deposition in the Beijing-Tianjin-Hebei region, China: Spatiotemporal characterization and regional source attributions, Atmos. Environ., 286, 119225, https://doi.org/10.1016/j.atmosenv.2022.119225, 2022.

Silver, B., Reddington, C. L., Arnold, S. R., and Spracklen, D. V.: Substantial changes in air pollution across China during
755 2015–2017, Environ. Res. Lett., 13(11), 114012, https://doi.org/10.1088/1748-9326/aae718, 2018.

Skamarock, W. C., Klemp, J. B., Dudhia, J., Gill, D. O.,Barker, D., Duda, M. G., Huang, X.-Y., Wang, W., and Powers, J. G.: A description of the advanced research WRF version 3, NCAR technical note, No. NCAR/TN-475CSTR, University Corporation for Atmospheric Research, https://doi.org/10.5065/D68S4MVH, 2008.

Smith, S. J., McDuffie, E. E., and Charles, M.: Opinion: Coordinated development of emission inventories for climate
760 forcers and air pollutants, Atmos. Chem. Phys., 22(19), 13201–13218, https://doi.org/10.5194/acp-22-13201-2022, 2022.

Son, K., Kim, B.-U., Kim, H. C., and Kim, S.: Source apportionment of ambient concentration and population exposure to elemental carbon in South Korea using a three-dimensional air quality model, Air. Qual. Atmos. Hlth., 15(10), 1729–1744, https://doi.org/10.1007/s11869-022-01213-z, 2022.

765 Souri, A. H., Choi, Y., Jeon, W., Li, X., Pan, S., Diao, L., and Westenbarger, D. A.: Constraining NO_x emissions using satellite NO_2 measurements during 2013 DISCOVER-AQ Texas campaign. Atmospheric Environment, 131, 371–381. https://doi.org/10.1016/j.atmosenv.2016.02.020, 2016.

Souri, A. H., Choi, Y., Jeon, W., Woo, J.-H., Zhang, Q., and Kurokawa, J.: Remote sensing evidence of decadal changes in major tropospheric ozone precursors over East Asia. Journal of Geophysical Research: Atmospheres, 122(4), 2474–
770 2492. https://doi.org/10.1002/2016JD025663, 2017.

Souri, A. H., Nowlan, C. R., González Abad, G., Zhu, L., Blake, D. R., Fried, A., Weinheimer, A. J., Wisthaler, A., Woo, J.-H., Zhang, Q., Chan Miller, C. E., Liu, X., and Chance, K.: An inversion of NO_x and non-methane volatile organic compound (NMVOC) emissions using satellite observations during the KORUS-AQ campaign and implications for surface ozone over East Asia, Atmos. Chem. Phys., 20(16), 9837–9854. https://doi.org/10.5194/acp-20-9837-2020,
775 2020.

Tang, B., Saide, P. E., Gao, M., Carmichael, G. R., and Stanier, C. O.: WRF-Chem quantification of transport events and emissions sensitivity in Korea during KORUS-AQ. Elementa-Sci. Anthrop., 11(1), 00096. https://doi.org/10.1525/elementa.2022.00096, 2023.

Wang, S., Zhang, Q., Martin, R. V., Philip, S., Liu, F., Li, M., Jiang, X., and He, K.: Satellite measurements oversee China's sulfur dioxide emission reductions from coal-fired power plants, Environ. Res. Lett., 10(11), 114015, https://doi.org/10.1088/1748-9326/10/11/114015, 2015.

Wang, C., An, X., Zhang, P., Sun, Z., Cui, M., and Ma, L.: Comparing the impact of strong and weak East Asian winter monsoon on $PM_{2.5}$ concentration in Beijing, Atmos. Res., 215, 165–177. https://doi.org/10.1016/j.atmosres.2018.08.022, 2019.

Wang, C.-Y., Chen, J.-P., and Wang, W.-C.: Meteorology-driven PM2.5 interannual variability over East Asia, Sci. Total. Environ., 904, 166911, https://doi.org/10.1016/j.scitotenv.2023.166911, 2023.

Wiedinmyer, C., Akagi, S. K., Yokelson, R. J., Emmons, L. K., Al-Saadi, J. A., Orlando, J. J., and Soja, A. J.: The Fire INventory from NCAR (FINN): A high resolution global model to estimate the emissions from open burning, Geosci. Model Dev., 4(3), 625–641, https://doi.org/10.5194/gmd-4-625-2011, 2011.

Woo, J.-H., Kim, Y., Kim, H.-K., Choi, K.-C., Eum, J.-H., Lee, J.-B., Lim, J.-H., Kim, J., and Seong, M.: Development of the CREATE inventory in support of integrated climate and air quality modeling for Asia. Sustainability-BaseL, 12(19), 7930. https://doi.org/10.3390/su12197930, 2020.

Wu, C.-H.: Seasonal adjustment of particulate matter pollution in coastal East Asia during the 2020 COVID lockdown, Environ. Res. Lett., 16(12), 124023, https://doi.org/10.1088/1748-9326/ac343c, 2021.

Wyrwoll, K.-H., Wei, J., Lin, Z., Shao, Y., and He, F.: Cold surges and dust events: Establishing the link between the East Asian Winter Monsoon and the Chinese loess record, Quaternary Sci. Rev., 149, 102–108. https://doi.org/10.1016/j.quascirev.2016.04.015, 2016.

Xian, Y., Zhang, Y., Liu, Z., Wang, H., and Xiong, T.: Characterization of winter $PM_{2.5}$ source contributions and impacts of meteorological conditions and anthropogenic emission changes in the Sichuan Basin, 2002–2020, Sci. Total. Environ., 947, 174557, https://doi.org/10.1016/j.scitotenv.2024.174557, 2024.

Xiu, A., and Pleim, J. E.: Development of a land surface model Part I: Application in a mesoscale meteorological model, J. Appl. Meteorol. Clim., 40(2), 192–209, https://doi.org/10.1175/1520-0450(2001)040<0192:DOALSM>2.0.CO;2, 2001.

Yuan, H., Dai, Y., Xiao, Z., Ji, D., and Shangguan, W.: Reprocessing the MODIS Leaf Area Index products for land surface and climate modelling, Remote Sens. Environ., 115(5), 1171–1187, https://doi.org/10.1016/j.rse.2011.01.001, 2011.

Yumimoto, K., Uno, I., and Itahashi, S.: Long-term inverse modeling of Chinese CO emission from satellite observations. Environ. Pollut., 195, 308–318, https://doi.org/10.1016/j.envpol.2014.07.026, 2014.

Zhai, S., Jacob, D. J., Wang, X., Shen, L., Li, K., Zhang, Y., Gui, K., Zhao, T., and Liao, H.: Fine particulate matter ($PM_{2.5}$) trends in China, 2013–2018: Separating contributions from anthropogenic emissions and meteorology, Atmos. Chem. Phys., 19(16), 11031–11041, https://doi.org/10.5194/acp-19-11031-2019, 2019.

810   Zhao, S., Feng, T., Tie, X., Li, G., and Cao, J.: Air Pollution Zone Migrates South Driven by East Asian Winter Monsoon and Climate Change, Geophys. Res. Lett., 48(10), e2021GL092672, https://doi.org/10.1029/2021GL092672, 2021.